ACS APPLIED ENERGY MATERIALS

www.acsaem.org

Article

Performance of Microporous Carbon Cathodes and Impact of Cathode/Solid Electrolyte Interphase Formation Using Carbonate and Ether-Based Electrolytes in Lithium−Sulfur Batteries

Delvina Japhet Tarimo, Francisco J. García-Soriano, Alen Vizintin, Christian Prehal, and Volker Presser*

Cite This: ACS Appl. Energy Mater. 2025, 8, 12139−12156

Read Online

ACCESS | Metrics & More | Article Recommendations | Supporting Information

ABSTRACT: Lithium−sulfur batteries (Li−S), controlled by the sulfur cathode's conversion reaction, are a promising technology due to their high theoretical capacities and the sustainability of sulfur. In contrast to commercially available lithium-ion cathodes, the Li−S system still suffers from unstable cycling performance due to the diffusion of soluble polysulfides out of the cathode. This study explored sulfur cathodes with varying pore sizes, mainly in the micropore regime (<2 nm). We conducted the work using carbonate-based and ether-based electrolytes to investigate the impact of the cathode/solid electrolyte interphase on the cycling performance of the battery. By infiltrating the carbon with different C/S ratios, we found that the maximum sulfur infiltration attained was 61 mass % with a C/S ratio of 1:1.5. The best sulfur utilization and cycling performance were achieved with carbonate electrolyte and 50 mass % S in carbon with a specific surface area of 2210 m^2/g and a total pore volume of 1.20 cm^3/g. Our findings emphasize the importance of designing cathodes with optimized pore structures to balance sulfur accommodation, minimize sulfur dissolution, and mitigate capacity degradation.

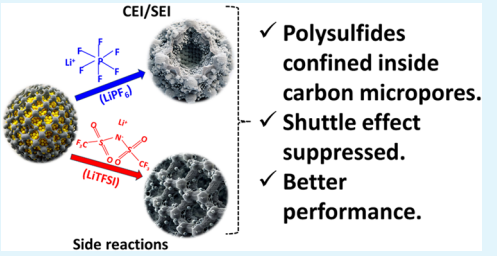

KEYWORDS: *lithium−sulfur batteries, polysulfide shuttling, carbonate-based electrolyte, sulfur loading, microporous carbon, electrolyte/sulfur ratio, energy storage*

1. INTRODUCTION

The increasing energy demand and the positive environmental impact of renewable energy require further development of high-capacity energy storage.[1−3] Lithium-ion batteries (LIBs) are often considered the core component of various portable electronic devices. However, the chemistries and materials employed in these batteries face safety concerns, high costs, and a limited theoretical energy density (350−400 Wh/kg), which hinders their ability to meet high-demand supply.[4] Various technologies are being researched to support the transition to more efficient energy storage technologies, address climate change, meet consumers' daily energy needs, and reduce high energy demand.[5−7] Current scientific research focuses on developing high-performance rechargeable batteries, which can potentially be realized through conversion-type reaction pathways using sulfur as a cathode.[8]

Lithium−sulfur batteries (Li−S) are a promising alternative to current LIBs because they use sulfur as the cathode material, which is inexpensive, nontoxic, and environmentally friendly.[9−11] The sulfur cathode has a high theoretical specific capacity of 1675 mAh/g, which is five times higher than the cathodes in commercial LIBs (300 mAh/g).[12] This results in a high theoretical specific energy of 2567 Wh per kilogram of active material.[13] Despite initial successes, Li−S batteries encounter challenges such as poor cell capacities due to low sulfur utilization and high electrolyte-to-sulfur ratios, as well as sluggish reaction kinetics resulting from the insulating properties of S_8 and the final discharge products (Li_2S).[14,15] More importantly, poor cycling stability is observed due to the formation of lithium dendrites, the shuttle effect of polysulfides, and the volume expansion of the cathode after lithiation, resulting in the pulverization of the cathode architecture during the discharging and charging processes.[16,17]

Various strategies have been employed to address these challenges and improve Li−S performance. One method is to trap sulfur in the cathode matrix, which serves as a physical barrier to encapsulate sulfur and facilitate efficient electron transport.[18,19] The high electrical conductivity, lightweight nature, and diverse porous structures rationalize this approach. However, studies suggest that carbon has a limited ability to inhibit the dissolution of polysulfide by trapping sulfur and its reduced forms at the cathode.[20] Therefore, carbon architecture is vital in harnessing the potential to restrict polysulfide dissolution. The formation of pores in the carbon material

Received: May 30, 2025
Revised: July 30, 2025
Accepted: July 31, 2025
Published: August 6, 2025

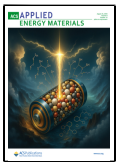

serves as an opening cavity for the impregnation and encapsulation of sulfur and redox products. According to international standards, pore size is classified as micropores (<2 nm), mesopores (2−50 nm), and macropores (>50 nm).[21] Due to their open porosity, carbons with macropores are ineffective in incorporating soluble polysulfides in Li−S.[22] Yet they are beneficial for sodium sulfur batteries (Na−S) to provide a free space for volumetric expansion of the redox reaction and enable the deposition of discharge products[23] because Na^+ has a larger ionic radius (0.95 nm) than Li^+ (0.60 nm).[24]

A study by Liu et al. on the influence of pore size and sulfur loading on the cycling performance of Li−S showed no direct relationship between the two parameters. This is because the prepared samples had a larger pore size, ranging from 3 to 22 nm, and exhibited the same initial sulfur utilization. However, they had a different weight ratio of sulfur, varying from 56% to 83%.[25] This study observed that the basic principle lies in the short chain of discharge products Li_2S_x ($2 \leq x \leq 4$), which contributes to achieving the theoretical capacity of Li−S.[25] Here, sulfur is usually confined in small micropores <0.7 nm, and the long-chain polysulfides Li_2S_x ($6 \leq x \leq 8$) are confined in the intermediate micropores of 0.76−0.84 nm.[26] For example, He et al. prepared bimodal carbons with different pore sizes ranging from 2.0 to 5.6 nm.[27] They observed that with increasing sulfur content, the smaller pores were preferentially filled during sulfur infiltration.[27] This shows that optimal sulfur content depends on the carbon host used, as the carbon porosity determines the amount of sulfur that can be efficiently infiltrated.[28,29] Consequently, microporous carbons are considered to have significant potential for producing sulfur cathodes. Sulfur confinement in the micropores is expected to reduce polysulfide shuttling and improve the cycling stability of the Li−S system.

Another approach to improve the Coulombic efficiency during cycling stability and ensure sulfur utilization is to stabilize the Li metal anode. Typically, lithium metal anodes encounter challenges in the application of Li−S due to their reaction with organic electrolytes, which form an unstable solid electrolyte interphase (SEI).[30] This leads to continuous irreversible consumption of active lithium, which limits cycling stability.[31] Therefore, researchers have considered modifying the electrolyte with various additives and solvents to stabilize the Li metal anode.[32,33] For the common ether-based electrolyte, one molar lithium bis(trifluoromethanesulfonyl)-imide in 1,3-dioxolane/1,2-dimethoxyethane (1 M LiTFSI in DOL/DME) with lithium nitrate ($LiNO_3$) as an additive, cutoff potentials of about 1.6−1.8 V vs Li/Li^+ to nearly 2.3−2.8 V vs Li/Li^+ are applied to avoid side reactions caused by $LiNO_3$.[34] Additionally, DOL/DME electrolytes have a low boiling point, and $LiNO_3$ serves as an oxidizing agent. Both raise safety concerns regarding operations at elevated temperatures.[35]

To overcome the challenges associated with state-of-the-art electrolytes, researchers are exploring carbonate-based electrolytes, which have already shown promising performance in LIBs.[36] It has the potential for higher oxidative stability, thermal stability with lower vapor pressure, and compatibility with Li-salts, creating a more stable cathode/solid electrolyte interphase (SEI/CEI). Despite the lower vapor pressure, carbonate-based electrolytes are chemically incompatible with most sulfur cathodes due to side reactions between carbonate solvents and polysulfide species. This results in poor cycling stability, reduced Li anode protection, and rapid electrolyte degradation.[37] However, carbonate electrolytes show promising performance when encapsulating short-chain sulfur molecules within a microporous carbon structure or by forming a strong chemical bond with a polymer host, employing high-concentration electrolytes or additives. These strategies result in good cycling performance yet minimal sulfur mass content (typically <40% by mass in the entire electrode).[38] In general, the practical performance of Li−S is reported to be highly sensitive to various manufacturing parameters, including cycling conditions, sulfur content, electrolyte/sulfur ratio, electrode thickness, areal sulfur loading, and electrolyte type.[39] While prior work has examined sulfur cathodes in various electrolytes, a systematic investigation of how well-defined cathode porosity affects sulfur confinement, dissolution behavior, and long-term capacity retention in both ether-based and carbonate-based electrolytes remains lacking.

The present study investigates the influence of atomic and nanoscale carbon structures on sulfur trapping within micropores and their impact on preventing polysulfide shuttling using ether- and carbonate-based electrolytes. Based on gas sorption analysis, X-ray diffraction (XRD), small-angle and wide-angle X-ray scattering (SAXS/WAXS), scanning electron microscope/energy-dispersive X-ray spectroscopy (SEM/EDX), and *ex situ* X-ray photoelectron spectroscopy (XPS) measurements, we analyze key parameters affecting capacities, cycle life, and sulfur loading. With our optimized sulfur cathode, we have achieved improved performance by using carbonate electrolytes, which have been reported to be incompatible with C/S cathodes without microporosity. The sulfur cathodes were prepared using a simple synthesis method and demonstrated promising performance, with a sulfur loading exceeding 50 mass %, utilizing a carbonate electrolyte. The importance of SEI formation for protecting Li metal anodes using a carbonate-based electrolyte is also discussed.

2. EXPERIMENTAL DESCRIPTION

2.1. Synthesis of Material and Electrode Preparation. Two commercial high specific surface area activated carbons, MSP20 (here called AC1, from Kansai Coke Chemical) and YP-50F (here named AC2, from Kuraray Chemicals), were used for initial electrochemical analysis to study the influence of the pore structure on reducing polysulfide formation on Li−S. The carbons were used as pristine samples, followed by activation. For sulfur infiltration, AC1 and sulfur (Sigma-Aldrich) were mechanically mixed at a mass ratio of 1:1 and ground in a ball mill at 300 rpm for 30 min. The mixture was then placed in a glass boat and heated under vacuum in a closed Büchi glass oven at 155 °C for 5 h. The resulting sample was abbreviated as AC1-S. The same sulfur infiltration procedure was performed on the AC2, and the sample was designated AC2-S. Both AC1-S and AC2-S were used as cathode materials in Li−S. The AC1-activated carbon was further activated with CO_2 at 800 and 1000 °C for 2 h (hereafter referred to as AC1−800 and AC1−1000, respectively) in a Xerion pendulum furnace using a quartz glass tube with a heating rate of 20 °C/min and a CO_2 flow of 100 mL/min. The tube was flushed with 200 mL/min of Ar during heating and cooling. The sulfur infiltration procedure was performed on the activated AC1−800 and AC1−1000, and the obtained samples were abbreviated as AC1−800-S and AC1−1000-S.

The electrodes consisted of carbon black type C65 (Imerys) and polyvinylidene fluoride (PVDF, molecular mass approximately 534 000 g/mol, Sigma-Aldrich) as a binder, in a mass ratio of 8:1:1. *N*-methyl-2-pyrrolidone (NMP, Sigma-Aldrich) was used as a solvent to prepare the slurry. The slurry was mixed in a ball mill at a speed of

https://doi.org/10.1021/acsaem.5c01629
ACS Appl. Energy Mater. 2025, 8, 12139−12156

300 rpm for 30 min, and then spread using a doctor blade with an automatic coater (MTI Mini Cast Coater MSK-AFA-HC100) onto carbon-coated aluminum foil. The slurry was dried in an oven at 80 °C for 12 h. The wet thickness was 200 μm, and the dried electrode attained a thickness of 80−90 μm with a mass loading of 2.6−3.8 mg/cm^2 (normalized by 80% of the active material in a 12 mm in diameter circular disc punched with El-Cut), which corresponds to a sulfur loading of (1.5−2.1) ± 0.3 mg/cm^2 (61 mass %).

2.2. Material Characterization. Nitrogen gas sorption analysis (GSA) at 77 K was performed using an Autosorb iQ system (Quantachrome; now Anton-Paar) to examine the porous structure of the synthesized samples. All samples were degassed at 200 °C under vacuum for 12 h. The porosity analysis was performed using quenched solid density functional theory (QSDFT), assuming a slit-shaped pore configuration. The average pore size was determined by the d_{50} value, which is the pore size equivalent to half of the pore volume.

XRD was performed using a D8 Advance diffractometer (Bruker AXS) with a copper source (Cu Kα, 40 kV, 40 mA). The X-ray beam was calibrated using the National Institute of Standards and Technology (NIST) 1976a corundum as the standard material. The measured signal was acquired using a 1D Lynxeye detector in 0.02° 2θ steps with a 1 s per step.

Raman analysis was performed using a Renishaw inVia Raman microscope, equipped with an Nd:YAG laser emitting at an excitation wavelength of 532 nm and a power of 0.5 mW at the focal point of the sample, with a numerical aperture of 0.75. For each sample, spectra from 5 points were recorded with a 10 s exposure time and accumulated 5 times. The spectra were normalized after treatment by removing cosmic rays.

The CHNS-O was used to study the chemical composition with a Vario Micro Cube system (Elementar Analysensysteme). After combustion, the samples were measured in a combustion tube under an oxygen atmosphere at 1150 °C. The CHNS-O analyzer was calibrated with sulfanilic acid (C: 41.6 mass %, H: 4.1 mass %, N: 8.1 mass %, and S: 18.5 mass %).

To compare the sulfur loading, thermogravimetric analysis (TGA) was performed using a Netzsch TG-209−1 Libra system to determine the mass changes in the temperature range of 30−550 °C at a heating rate of 10 °C/min under Ar gas. The ranges were selected as sulfur sublimates when heated to 450 °C at ambient pressure.

We used a ZEISS Gemini 500 SEM and an Xmax detector from Oxford Instruments for EDX analysis. The system was operated at an acceleration voltage of 1 kV for imaging and 10 kV for spectroscopy. An aluminum stub and copper tape were used as a substrate to attach the samples. At least 20 points were selected randomly for elemental analysis, and the average amount of elements detected was calculated.

SAXS/WAXS was used to study the nanopore structure of the produced carbons and the sulfur pore filling. The measurement of the noninfiltrated and sulfur-infiltrated powder samples in a vacuum was carried out using the Xeuss 3.0 laboratory SAXS/WAXS system from Xenocs with Cu−Kα radiation (wavelength, λ = 0.154 nm) and the single photon counting detector Eiger 2R 1 M from Dectris. The WAXS data were calculated by converting the q-data into two theta using the following equation

$$\text{two theta } (2\theta) = 2\arcsin\left[\frac{(q \times \lambda)}{(4 \times \pi)}\right] \quad (1)$$

where λ is the wavelength of the Cu−Kα radiation in Angström.

The carbon−sulfur cathodes and lithium anode were studied using XPS after galvanostatic cycling under the same conditions as the electrochemical tests. These measurements were performed on the electrodes after the first and 10th discharge cycles. The cells were disassembled inside a glovebox and dried under dynamic vacuum overnight to conduct these studies. The samples were then transferred to the vacuum transfer module, an accessory of the Versa probe 3 AD, ensuring no air exposure.

XPS analysis was conducted using a Versa probe 3 AD (Physical Electronics) with an Al−Kα_1 X-ray excitation source (1486.7 eV), operating monochromatically at 46.0 W. Measurements were performed at room temperature under high vacuum (10^{-7} Pa), and the spectra were acquired by scanning a 1 mm^2 area with a beam size of 200 μm. A charge neutralizer was used since the samples were mounted on nonconductive double tape to prevent shifts in the charge state of the electrodes. Survey spectra, along with core-level spectra for phosphorus (P 2p), sulfur (S 2p), carbon (C 1s), nitrogen (N 1s), oxygen (O 1s), and fluorine (F 1s), were collected for detailed analysis. The pass energy and energy resolution were set to 224 and 0.8 eV for the survey scans and 27 and 0.05 eV for the core-level spectra. Voigt functions were used for spectral deconvolution, using Ulvac-PHI Multipak software, with Shirley background correction applied to all spectra. The binding energy scale was calibrated using Au 4f = 83.99 eV from pristine gold, which was sputtered for 7 min to remove possible impurities. Three regions were analyzed for each sample to ensure statistical accuracy and avoid potential single-point interpretations.

2.3. Electrochemical Analysis. To study the electrochemical behavior of the produced cathode material, a CR2032 coin cell was used to fabricate Li−S cells. Cells were assembled in an Ar-filled glovebox (MBraun with O_2 and H_2O < 0.1 ppm) using Li metal foil (11 mm diameter and 0.025 mm thickness) as counter electrode and reference electrode with Celgard 2320 separator. A minimum of three cells were assembled for each cathode/parameter under study to ensure reproducibility. During cell assembly, 40 μL/mg$_s$ of ether-based electrolyte, 1 M LiTFSI + 0.25 M $LiNO_3$ in DOL/DME (1:1 by volume) was used and compared with carbonate-based electrolyte; 1 M $LiPF_6$ in fluoroethylene carbonate (FEC): dimethyl carbonate (DMC) (1:4 by volume) (LiTFSI, $LiNO_3$, DOL (99.8%), DME (99.5%), $LiPF_6$, FEC (99.99%) and DMC (≥99%) were from Sigma-Aldrich). A higher amount than 4−5 μL/mg$_S$ of electrolyte was used to prevent cathode swelling due to electrolyte uptake and subsequent drying.[40−42] The galvanostatic charge/discharge experiments were carried out to examine the cycling stability in Biologic VMP-300 potentiostat/galvanostat at C/20 in a voltage range of 0.5−3.0 V vs Li/Li$^+$ for five formation cycles and then C/10 in a potential range of 1.0−3.0 V vs Li/Li$^+$ in the subsequent cycles (1C = 1672 mAh/g$_s$). All electrochemical experiments were performed in a climate-controlled chamber maintained at 25 ± 1 °C. Unless specified otherwise, we calculated the capacity values based on the active material (sulfur). The Coulombic efficiency was calculated by dividing the discharge capacity by the previous charge capacity. Cyclic voltammetry was performed in a potential range of 1.0−3.0 V vs Li/Li$^+$ at 0.1 mV/s. In comparison, electrochemical impedance spectroscopy (EIS) was measured at open-circuit voltage (OCV) in a frequency range of 10 kHz to 10 mHz. The cells were rested for 2 h before EIS measurements.

3. RESULTS AND DISCUSSION

3.1. Electrochemical Performance of the Initial Carbon Materials. An initial electrochemical analysis was conducted to assess the suitability of porous carbon for mitigating the polysulfide shuttle on two carbons, AC1-S and AC2-S, as described in Section 2.1. These carbons were chosen for their high SSA and easily adjustable pore volume. The measurements were carried out in 1 M $LiPF_6$ in FEC/DMC (1:4 by volume) carbonate-based electrolyte. Supporting Information, Figure S1A shows the first cycle discharge and charge profiles of AC1-S and AC2-S at a lower cutoff potential of 0.5−3.0 V vs Li/Li$^+$ with a rate of 0.05C. The AC1-S recorded a specific capacity of 1106 mAh/g$_s$, while for AC2-S, a value of 1018 mAh/g$_s$ at 0.05C was obtained. The AC1-S and AC2-S cells were cycled at a rate of 0.05C for 5 cycles and later cycled at a higher cutoff potential of 1.0−3.0 V vs Li/Li$^+$ with a rate of 0.1C. Supporting Information, Figure S1B shows the cycling stability of AC1-S and AC2-S at 0.1C, displaying an initial discharge capacity of 804 mAh/g$_s$ and 631 mAh/g$_s$ for

https://doi.org/10.1021/acsaem.5c01629
ACS Appl. Energy Mater. 2025, 8, 12139−12156

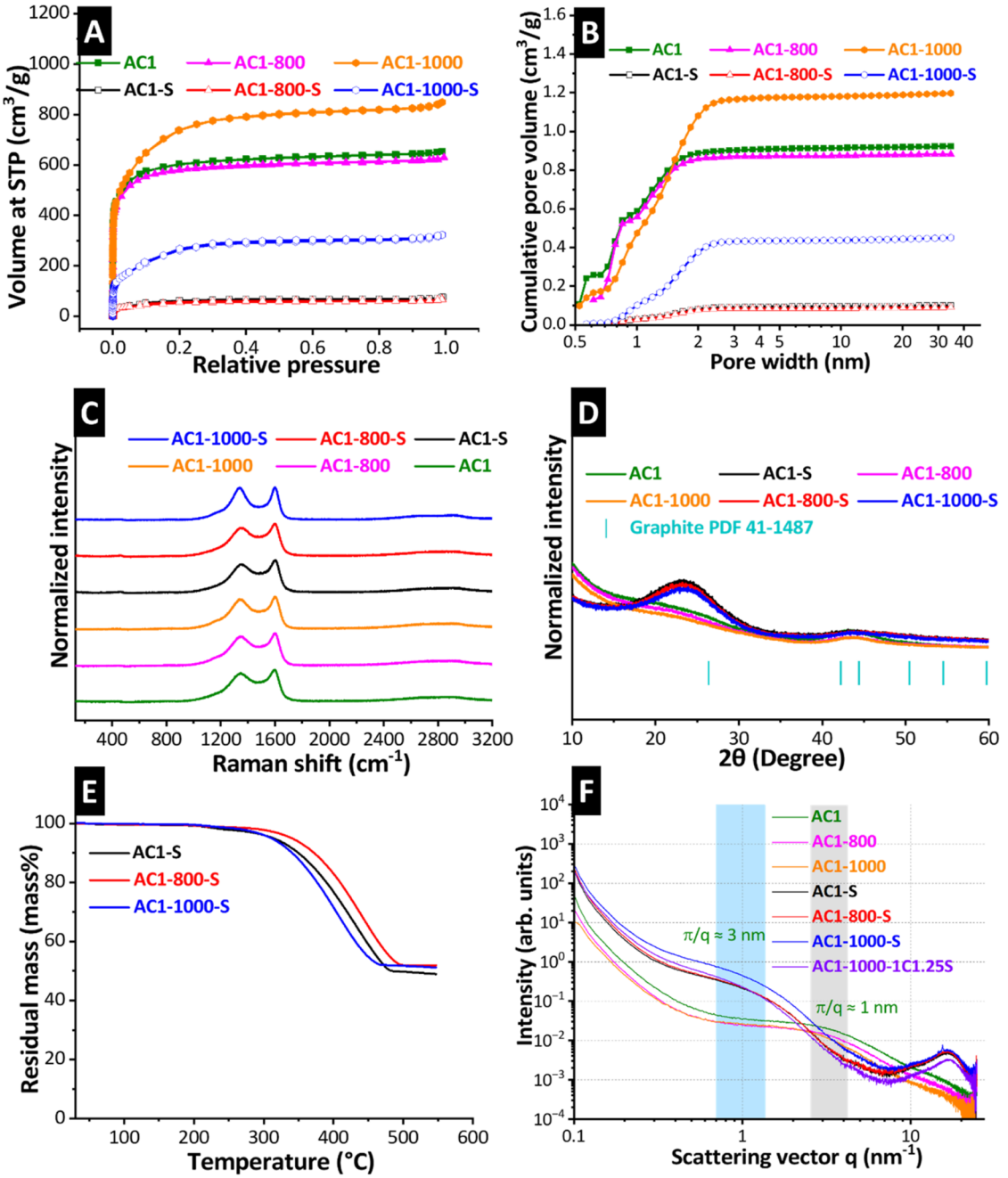

Figure 1. Nitrogen sorption isotherms at −196 °C (A), calculated pore size distributions derived from nitrogen gas sorption (B), Raman spectra (C), and X-ray diffractograms (D) for AC1, AC1−800, AC1−1000, AC1-S, AC1−800-S, and AC1−1000-S samples. Thermogravimetric analysis to calculate sulfur content in AC1-S, AC1−800-S, and AC1−1000-S (E), and small-angle X-ray scattering intensity versus scattering vector length Q (F) of the optimized pore structures AC1, AC1−800, and AC1−1000, as well as the sulfur infiltrated samples AC1-S, AC1−800-S, AC1−1000-S, and AC1−1000−1C1.25S.

AC1-S and AC2-S, respectively. Cells were cycled for 100 cycles. According to the results shown in the Supporting Information, Figure S1B, after the first 5 cycles, there is an initial decrease in discharge capacity due to the switch to the higher rate. The reaction kinetics in the solid-to-solid region are very slow, leading to high polarizations.[43] Following recent work,[44] we used a lower potential of 0.5−3.0 V vs Li/Li^+ with 0.05C to facilitate the transition to Li_2S and CEI formation for the carbonate electrolyte.[45] After five initial formation cycles, a higher cutoff potential of 1.0−3.0 V vs Li/Li^+ at a higher rate of 0.1C was chosen for the subsequent cycles to analyze the cycling stability of the two types of activated carbons. The results show that the discharge capacity of AC2-S decreases sharply as the number of cycles increases compared to AC1-S (Supporting Information, Figure S1B). The results also suggest that AC1-S exhibits better cycling stability, as 536 mAh/g_s was measured after 100 cycles, compared to 261 mAh/g_s for AC2-S. In addition, during charging, the AC1-S exhibits a lower onset voltage, thereby reducing the voltage gap, which indicates reduced polarization and faster conversion kinetics.

Based on this analysis, AC1-S was selected for further modifications to investigate the effect of increased porosity by

https://doi.org/10.1021/acsaem.5c01629
ACS Appl. Energy Mater. 2025, 8, 12139−12156

Table 1. Surface and Pore Structure Analysis of Non-Activated AC1, Activated AC1-800, and AC1-1000, along with Their Corresponding Infiltrated AC1-S, AC1-800-S, and AC1-1000-S

sample name	treatment	DFT SSA (m^2/g)	average pore size d_{50} (nm)	micropore volume (cm^3/g)	mesopore volume (cm^3/g)	total pore volume (cm^3/g)
AC1	as received	2210	0.8	0.89	0.04	0.92
AC1−800	CO_2 activation at 800 °C	2005	0.8	0.86	0.02	0.88
AC1−1000	CO_2 activation at 1000 °C	2246	1.2	1.08	0.12	1.20
AC1-S	as received, after sulfur-infiltration	152	1.4	0.08	0.02	0.10
AC1−800-S	CO_2 activation at 800 °C, after sulfur-infiltration	140	1.3	0.08	0.01	0.09
AC1−1000-S	CO_2 activation at 1000 °C, after sulfur-infiltration	648	1.4	0.38	0.07	0.45

Table 2. Chemical Composition of Sulfur-Infiltrated Carbons[a]

	CHNS-O chemical analysis					TGA
sample name	C	N	H	O	S	S
AC1-S	47.1 ± 0.0	1.3 ± 0.0	0.5 ± 0.0	-	52.9 ± 0.2	50
AC1−800-S	47.7 ± 0.3	1.2 ± 0.4	-	3.3 ± 0.4	51.6 ± 0.3	48
AC1−1000-S	49.4 ± 1.3	1.9 ± 0.2	-	2.8 ± 0.1	50.4 ± 0.4	49
AC1−1000−1C1.25S	42.3 ± 0.7	-	0.2 ± 0.1	2.4 ± 0.3	57.0 ± 1.4	53
AC1−1000−1C1.5S	38.4 ± 0.4	-	0.2 ± 0.0	2.5 ± 0.2	61.0 ± 1.5	56

[a]All values in mass %. S mass loss from TGA is calculated from the difference between the mass remaining and the original (100%).

CO_2 activation on the uptake of the polysulfide species and its influence on cycling stability. In addition, the activation aimed to increase the pore volume, thereby creating space for easy Li^+ migration and sulfur inclusion in the micropores, which prevents polysulfide shuttling and improves the cycling stability of Li−S.

3.2. CO_2 Activation and Pore Structure Modification.

Based on the above discussion, we selected AC1 to investigate the formation of CEI and polysulfide shuttling through pore variations. The AC1 was subjected to CO_2 activation at 800 and 1000 °C for 2 h to modify the carbon porosity, followed by sulfur infiltration. All activated samples, namely AC1, AC1−800, and AC1−1000, as well as the infiltrated samples AC1-S, AC1−800-S, and AC1−1000-S, were analyzed by nitrogen gas sorption analysis (GSA) performed at −196 °C (Figure 1A,B). The nitrogen sorption isotherms confirmed the dominance of micropores for all samples, with a higher increase in pore volume for the sample activated at 1000 °C (AC1−1000). The pore size distribution was calculated using a QSDFT model assuming slit-shaped pores (Figure 1B). The DFT SSA of 2210 m^2/g, 2005 m^2/g, and 2246 m^2/g was recorded for AC1, AC1−800, and AC1−1000, respectively. The average pore size of AC1 was 0.8 nm with a total pore volume of 0.92 cm^3/g. The average pore size of AC1−800 remained similar to AC1 (0.8 nm with a total pore volume of 0.88 cm^3/g) and increased to 1.2 nm (total pore volume of 1.20 cm^3/g) after CO_2 activation at 1000 °C (AC1−1000), as shown in Table 1. The lower CO_2 activation temperature of 800 °C does not change the specific pore volume (Table 1) because the activation rate of the CO_2 reaction with the carbon matrix is very slow. Thus, the activation step requires a higher temperature for the formation of larger micropores.[46,47] After sulfur infiltration, the DFT SSA decreased to 152 m^2/g, 140 m^2/g, and 648 m^2/g for AC1-S, AC1−800-S, and AC1−1000-S, respectively. This trend is also observed in their respective total pore volume and micropore volume, as shown in Table 1. Hence, smaller pores are initially filled during the sulfur infiltration process. DFT calculations showed that the long-chain polysulfides of LiS_8 and Li_2S_6 molecules have a diameter of 0.84 and 0.76 nm, while the short-chain polysulfides Li_2S_2−Li_2S_4 have a dimension of <0.5 nm.[48,49] In this context, micropores of AC1, AC1−800, could accommodate more short-chain polysulfides while AC1−1000 could accommodate both polysulfide molecules.

3.3. Structural Analysis and Chemical Composition.

Raman spectra and X-ray diffractograms were recorded to characterize the carbon structure. The Raman spectra (Figure 1C) displayed the D-band (1344 cm^{-1}) and G-band (1597 cm^{-1}) in AC1, AC1−800, and AC1−1000 samples, the two significant peaks for the carbon materials.[50] The D-band arises from defects within the carbon structure, while the G-band is associated with the sp^2 hybridization of the symmetric stretching mode of graphitic domains.[51] For AC1-S, AC1−800-S, and AC1−1000-S samples, no peak was visible in the spectral range below 500 cm^{-1}. The absence of these vibrations, combined with the presence of sulfur as indicated by chemical analysis, suggests that sulfur was confined to the porous carbon matrix. This was also confirmed by scanning electron micrographs in Supporting Information, Figure S2A−F, as the shape and size of the particles are preserved. There are no traces of sulfur particles on the outer surface of the carbon. Additionally, sulfur trapped in micropores was evident through defects in the carbon structure, both before and after sulfur infiltration. The defect (Figure 1C) was evaluated by calculating the I_D/I_G ratio using the Voigt function. The AC1-S and AC1−800-S presented a similar I_D/I_G ratio of 1.16 (Supporting Information, Table S1). Conversely, the AC1−1000-S showed a higher I_D/I_G ratio of 1.19, signifying higher defects and more disordered structures.[52]

This trend was also confirmed by X-ray diffraction results in Figure 1D, which shows two broad carbon peaks at 24° and 43° 2θ for AC1, AC1−800, and AC1−1000 samples. These reflections show the presence of incomplete crystalline graphitic carbon. The peaks are indexed with the characteristic peaks of graphite (PDF number 41−1487) of the (002) and (100) planes, respectively.[53] The absence of a sharp crystalline sulfur peak in the X-ray diffractograms confirms the observations from SEM and Raman analysis, which show

https://doi.org/10.1021/acsaem.5c01629
ACS Appl. Energy Mater. 2025, 8, 12139−12156

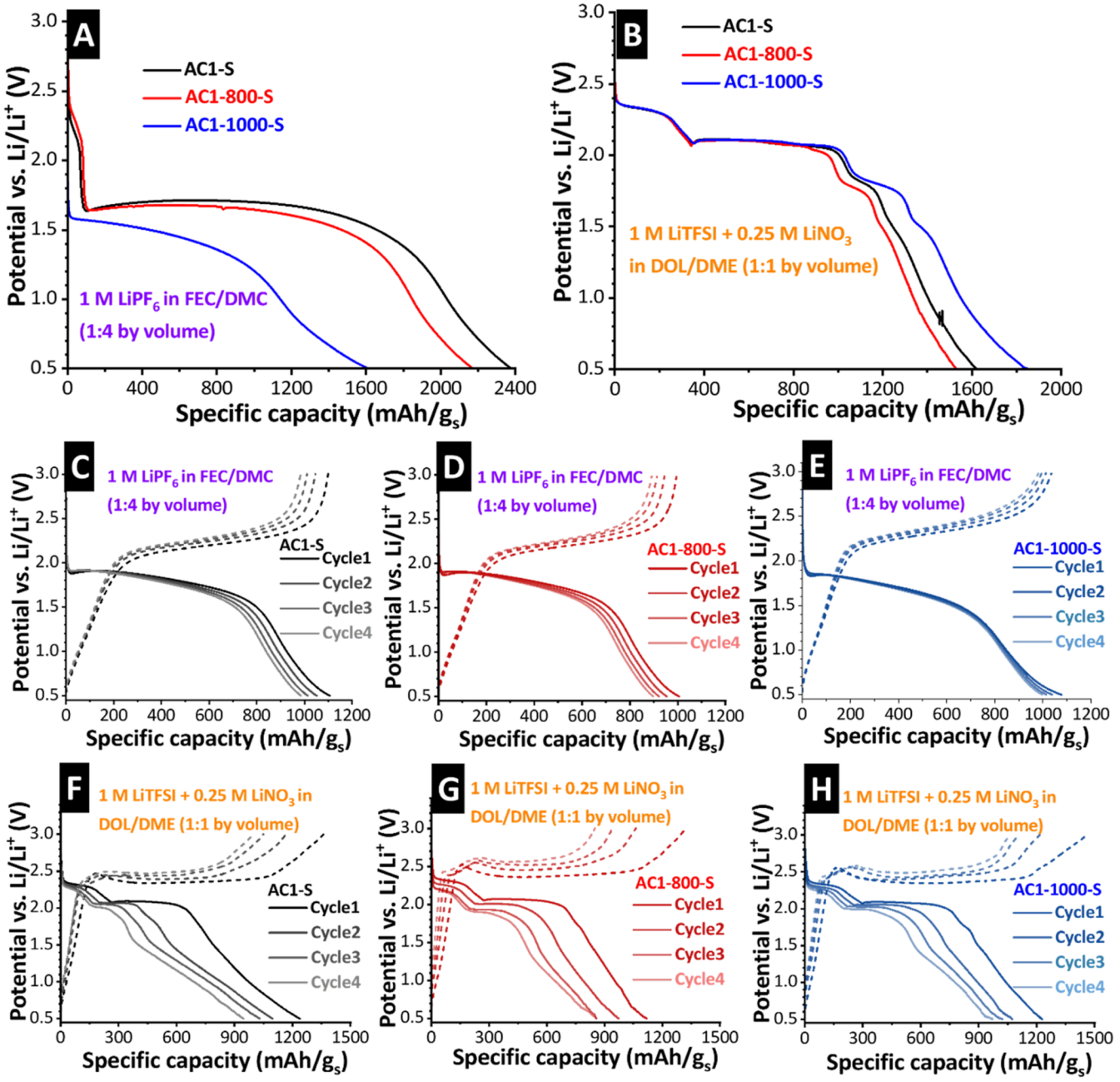

Figure 2. Initial discharge of AC1-S, AC1−800-S, and AC1−1000-S in a carbonate-based electrolyte (A) and an ether-based electrolyte (B). The charging and discharging of cycles one to four for AC1-S, AC1−800-S, and AC1−1000-S in the carbonate-based electrolyte (C−E) and the ether-based electrolyte (F−H).

that sulfur is amorphous and likely infiltrated inside the micropores of the carbon matrix.

Thermogravimetric analysis (TGA) was performed to examine the amount of sulfur infiltrated into the carbon samples. The measurement was executed between 30 and 550 °C under argon gas, with the sulfur expected to completely evaporate at 450 °C. Expectedly, sulfur did not completely evaporate at 450 °C as it was confined within the porous carbon matrix, and a higher temperature was required for mobilization and evaporation.[54] As seen in Figure 1E, based on the recorded mass loss, the amount of sulfur was 50 mass %, 48 mass %, and 49 mass % for AC1-S, AC1−800-S, and AC1−1000-S, respectively. The amount of sulfur was also confirmed by CHNS-O analysis to be 53 mass %, 52 mass %, and 50 mass % for AC1-S, AC1−800-S, and AC1−1000-S, respectively (Table 2). All samples exhibit nitrogen levels below 2 mass % and oxygen levels below 3 mass % for AC1−800-S and AC1−1000-S.

The AC1−1000 with a higher pore volume (1.20 cm^3/g) was further infiltrated with a higher amount of sulfur to gain insight into the maximum sulfur content that can be infiltrated in this carbon. The carbon was loaded with the carbon−sulfur ratio of C:S = 1:1.25 and C:S = 1:1.5. The sulfur content was determined by TGA analysis to be 53 mass % and 56 mass % for AC1−1000−1C1.25S and AC1−1000−1C1.5S, respectively (Supporting Information, Figure S3A). The sulfur content was confirmed by CHNS analysis to be 57 mass % for AC1−1000−1C1.25S and 61 mass % for AC1−1000−

https://doi.org/10.1021/acsaem.5c01629
ACS Appl. Energy Mater. 2025, 8, 12139−12156

1C1.5S. There are no additional sulfur-related reflections, including the X-ray diffractograms of AC1−1000−1C1.25S and AC1−1000−1C1.5S samples (Supporting Information, Figure S3B). TGA analysis showed a small fraction of surface sulfur on the carbon particles for the higher sulfur contents (Supporting Information, Figure S3A). Specifically, in AC1−1000−1C1.5S, the sulfur evaporation started at a lower temperature than in-pore sulfur in the AC1−1000−1C1S and AC1−1000−1C1.25S samples. These results are consistent with our pore structure analysis in Section 3.2 and Table 1, which indicate that the small pores are filled first; however, as the amount of sulfur increases, the pores become saturated. Some of the sulfur is also present outside the carbon structure.

To verify the mean pore sizes as well as sulfur pore filling inside the nanopores, we conducted SAXS/WAXS analysis. Figure 1F and Supporting Information, Figure S3C displays SAXS and WAXS results of AC1, AC1−800, AC1−1000, AC1-S, AC1−800-S, AC1−1000-S and AC1−1000−1C1.25S. The position of the SAXS intensity shoulder is related to the mean pore size ($d_{50} \approx \pi/q$ indicated by the light gray area) and aligns with the trends obtained from gas sorption analysis. AC1 and AC1−800 have a similar mean pore size, while AC1−1000 shows a slightly increased pore size. Upon filling the carbons with sulfur, the SAXS intensity hump shifts toward lower q-values. Interestingly, the q-position indicates a mean feature size of $\pi/q \approx 3$ nm, which is much larger than the mean pore size. This suggests that the sulfur does not simply fill the pores randomly but forms some larger superstructure inside the activated carbon particles. We do not expect this sulfur structure to play a significant role for standard ether-based electrolytes, given the complete dissolution of sulfur into polysulfides; however, for carbonate electrolytes, we expect that the initial sulfur structure impacts the active material/CEI composite structure after the formation cycles. The WAXS data (Supporting Information, Figure S3C) show a broad peak around 25° 2θ, indicating the presence of amorphous sulfur in the sulfur-infiltrated samples, which is in line with the XRD measurements.

3.4. Electrochemical Performance of Lithium−Sulfur Batteries. The activated carbon materials were investigated as cathodes (AC1-S, AC1−800-S, and AC1−1000-S) for Li−S batteries, as described in Section 2.1. The cathodes were first examined in 1 M $LiPF_6$ in FEC/DMC, 1:4 by volume (carbonate-based electrolyte), and 1 M LiTFSI + 0.25 M $LiNO_3$ in DOL/DME, 1:1 by volume (ether-based electrolyte) to understand the irreversible capacity loss caused by the reaction of polysulfides and the selected electrolytes. The amount of electrolyte was calculated based on the sulfur content in each sample. All electrochemical measurements were performed using 40 $\mu L/mg_S$ to avoid electrolyte limitation and ensure adequate sulfur utilization. Measurements were performed at C/20 in a potential range of 0.5−3.0 V vs Li/Li^+ for five formation cycles and then at C/10 in a potential range of 1.0−3.0 V vs Li/Li^+ in the subsequent cycles (1C = 1675 mAh/g_s).

Figure 2A displays the initial discharge profiles of AC1-S, AC1−800-S, and AC1−1000-S in the carbonate-based electrolyte executed at C/20 in a potential range of 0.5−3.0 V vs Li/Li^+. Two plateaus are observed for AC1-S and AC1−800-S, with the first minor plateau at 2.37 V vs Li/Li^+ corresponding to 73 mAh/g_S and the second plateau at 1.63 V vs Li/Li^+ corresponding to 2376 mAh/g_s for AC1-S and 2169 mAh/g_S for AC1−800-S. AC1−1000-S displayed only a plateau at 1.60 V vs Li/Li^+ with a 1615 mAh/g_S length. The formation of the first plateau for AC1-S and AC1−800-S is associated with the formation of long-chain polysulfide intermediate species that react with the carbonate electrolyte solvents.[55] The length of the second plateau for AC1-S and AC1−800-S is higher than the theoretical specific capacity of sulfur (1675 mAh/g_s), which is associated with the CEI formation and the decomposition of the electrolyte.[56] The single plateau length of AC1−1000-S was close to the theoretical specific capacity of sulfur, with a slight difference of 57 mAh/g_s. During the initial discharge capacity of the Li−S system, CEI formation occurs due to the reaction between the C/S cathode and the carbonate electrolyte solvents.[57] The layer formed consumes sulfur as the active material involved in the electrochemical reactions and can vary in thickness, depending on the amount of polysulfide species, creating an additional barrier that slows down the reaction kinetics. As a result, part of the sulfur is already consumed in the reversible reactions, leading to a low specific capacity in subsequent cycles. The formed CEI layer appears to mitigate polysulfide shuttling.[58] However, this also depends on the physicochemical properties of the sulfur cathode. Our AC1-S and AC1−800-S, which possess a similar I_D/I_G ratio of 1.16 and have a similar mean pore size of 0.8 nm in their carbon structures, displayed two plateaus. While the AC1−1000-S has a slightly higher I_D/I_G ratio of 1.19, suggesting additional defects and more disordered structures with a carbon structure characterized by a higher mean pore size of 1.2 nm, it exhibits a single plateau. The single plateau is associated with the full confinement properties of the microporous structure, whose reaction is a quasi-solid-state process.[45] The nanoconfinement restricts the growth and mobility of polysulfides, and forms a compact CEI that passivates the surface of AC1−1000-S and adjusts its electrochemical properties, resulting in a single plateau.[59] This effect is expected to enhance the electrochemical performance of AC1−1000-S more than that of AC1-S and AC1−800-S. This is also confirmed by DFT calculations and our designed pore structure, which shows that AC1 and AC1−800 with a pore diameter of 0.8 nm can accommodate more short-chain polysulfides, Li_2S_2−Li_2S_4 (<0.5 nm). In comparison, AC1−1000 with a 1.2 nm pore diameter could accommodate both polysulfides (LiS_8: 0.84 nm and Li_2S_6: 0.76 nm).[26] The cyclic voltammograms of all samples in the carbonate-based electrolyte performed at 0.1 mV/s in a potential range of 1.0−3.0 V vs Li/Li^+ further confirmed the behavior of these plateaus (Supporting Information, Figure S4A). To investigate this phenomenon further, we analyzed the charging and discharging of the four cycles in our cathodes (AC1-S, AC1−800-S, and AC1−1000-S).

Figure 2C−E shows the first to fourth charge/discharge cycles for AC1-S, AC1−800-S, and AC1−1000-S at C/20 in a potential range of 0.5−3.0 V vs Li/Li^+. The discharge curve reveals a single plateau for all samples. This behavior confirms the chemical reaction between Li−S and the microporous carbon in a carbonate-based electrolyte.[55] The AC1-S delivered a specific discharge capacity of 1106 mAh/g_S to 985 mAh/g_S for cycles one to four, as shown in Figure 2C. Figure 2D presents the specific discharge capacity of 1006 mAh/g_S to 898 mAh/g_S for cycles one to four for AC1−800-S, while the AC1−1000-S in Figure 2E recorded a specific discharge capacity of 1077 mAh/g_S to 997 mAh/g_S, for cycles 1 to 4. The specific capacities are lower than the theoretical

https://doi.org/10.1021/acsaem.5c01629
ACS Appl. Energy Mater. 2025, 8, 12139−12156

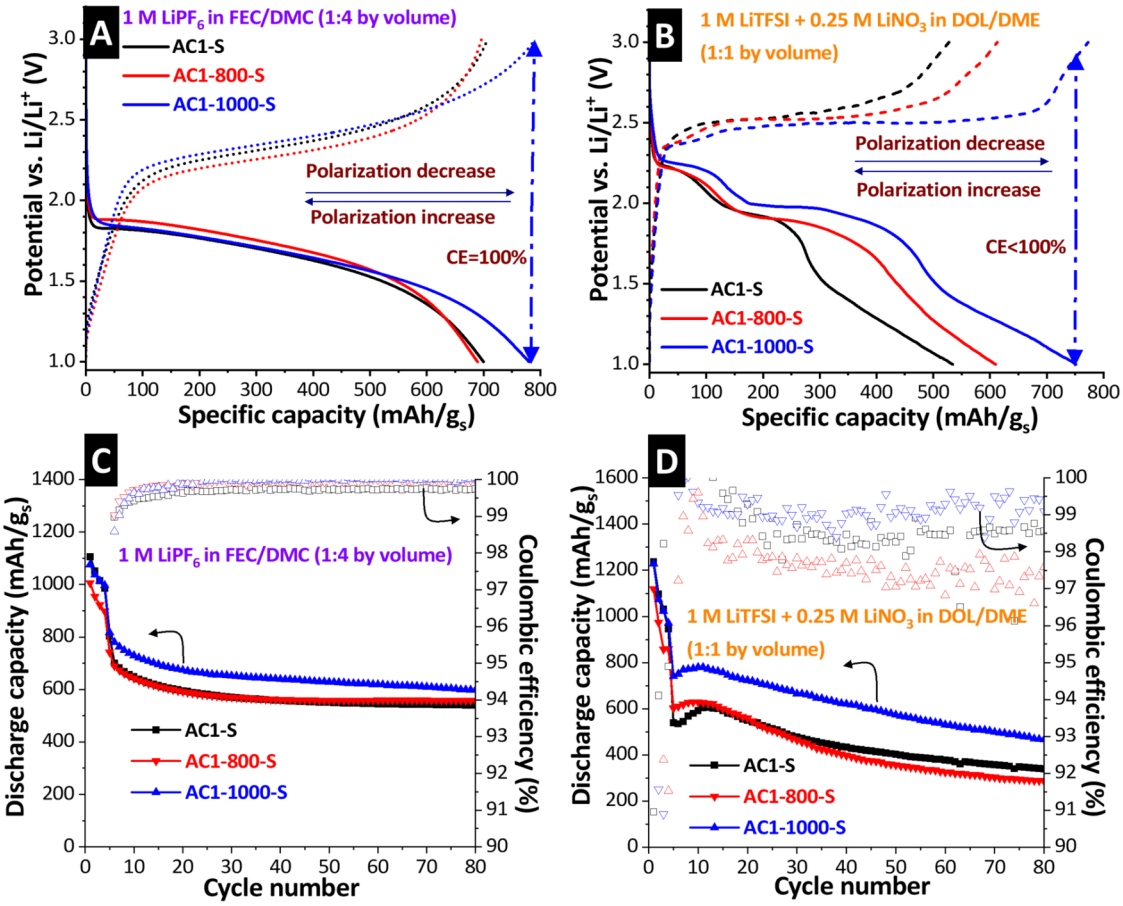

Figure 3. Charging and discharging of cycle five at 0.1C for AC1-S, AC1−800-S, and AC1−1000-S in a carbonate-based electrolyte (A) and an ether-based electrolyte (B), showing the polarization effect. The cycling stability and Coulombic efficiency of AC1-S, AC1−800-S, and AC1−1000-S in a carbonate-based electrolyte (C) and an ether-based electrolyte (D) for 80 cycles.

capacity of sulfur because some of the active materials were consumed during CEI formation, Li metal side reactions, or losses due to confinement and conductivity limitations within the micropores. Besides, both samples exhibit good reversibility in the carbonate-based electrolyte, as they display nearly the same discharge capacity in the first cycle, indicating that sulfur utilization in a full pore was similar for both. This performance is consistent with the sulfur content of AC1-S, AC1−800-S, and AC1−1000-S measured by CHNS and TGA, as shown in Table 2. Furthermore, the performance behavior of AC1-S, AC1-S, and AC1−1000-S was found to be consistent with the behavior of the initial discharge analysis. Although AC1-S had a slightly higher discharge capacity in the first cycle, the capacity decay rate in the subsequent cycles was higher than that of AC1−1000-S. The AC1−1000-S exhibits good stability, sustaining a specific discharge capacity of more than 1000 mAh/g_S over four cycles, which is higher than that of the AC1-S and AC1−800-S, as shown in Figure 2E.

The performance of AC1−1000-S in the initial discharge and subsequent cycles can be explained as follows: (1) The enhanced porous structure creates space for large volume change during charge/discharge and sulfur enclosure in the micropores, thus preventing polysulfide shuttling; (2) The upper plateau was sustained as the number of cycles increased, indicating efficient utilization of the active materials without degradation and (3) CEI formation reduce the side reactions associated with the dissolution of polysulfide species in the electrolyte during the reversible reactions. The slow decrease in discharge capacity for AC1-S and AC1−800-S in cycles one to four indicates that these electrodes lack sufficient channels (limited by their porosity) for lithium ions to traverse, and low interfacial contact thus affects the electrochemical reactions.

Figure 2B shows the initial discharge profiles of AC1-S, AC1−800-S, and AC1−1000-S in 1 M LiTFSI + 0.25 M $LiNO_3$ in DOL/DME (1:1 by volume) ether-based electrolyte performed at C/20 in a potential range of 0.5−3.0 V vs Li/Li^+. Despite the $LiNO_3$ decomposition below 1.8 V vs Li/Li^+, we discharge the cell at a lower voltage to (1) examine whether the produced microporous confine the polysulfides reactions using an ether-based electrolyte, (2) to facilitate the complete transition to Li_2S and CEI formation and (3) to compare the electrochemical performance of the produced microporous carbon in the standard ether-based electrolyte and the proposed carbonate electrolyte within the same potential range. Four plateaus are observed for AC1-S, AC1−800-S, and AC1−1000-S, with the first plateau at 2.4 V vs Li/Li^+ with a length of 346 mAh/g_s, indicating the formation of long-chain polysulfides from sulfur and the formation of short-chain polysulfides in the sloping region.[60] The second plateau formed at 2.0 V vs Li/Li^+ with a length between 1530 and 1840 mAh/g_s, presenting the equilibrium between the short-chain polysulfide and Li_2S formation.[48] The two plateaus below 1.8 V are due to $LiNO_3$ decomposition at the Li anode and/or cathode surface and polysulfide reduction, where the

https://doi.org/10.1021/acsaem.5c01629
ACS Appl. Energy Mater. 2025, 8, 12139−12156

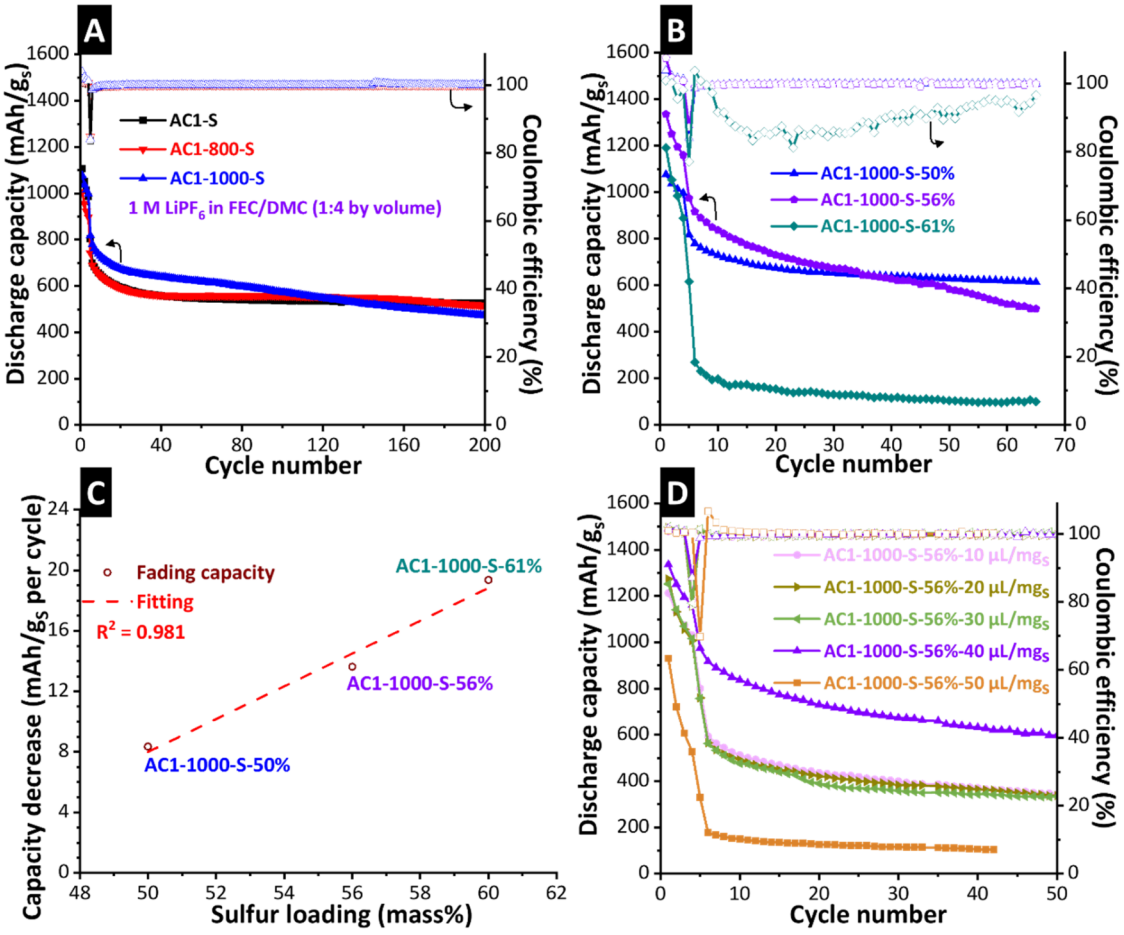

Figure 4. Cycling stability and Coulombic efficiency of AC1-S, AC1−800-S, and AC1−1000-S in a carbonate-based electrolyte for 200 cycles at 0.1C (A). The cycling stability and Coulombic efficiency of AC1−1000 with higher loading AC1−1000-S-56% and AC1−1000-S-61% compared to AC1−1000-S-50% in a carbonate-based electrolyte for 50 cycles (B). The capacity fading rate is calculated from panel (B) (C), and the discharge capacity of AC1−1000-S-56% is calculated using different amounts of electrolytes (D).

overlay of sulfur reduction peaks is reduced with a higher solubility of polysulfide, causing the loss of active material.[34] This results in irreversible reductions in the utilization of active materials, capacity drop, and low Coulombic efficiency.[61] The cyclic voltammograms of all samples showed similar behavior in the ether-based electrolyte, confirming the behavior of these plateaus (Supporting Information, Figure S4B).

To analyze the behavior of these plateaus, the cells were subjected to charge/discharge over the next four cycles. Figure 2F−H shows the charge/discharge cycles one to four for AC1-S, AC1−800-S, and AC1−1000-S at C/20 in a potential range of 0.5−3.0 V vs Li/Li$^+$. The specific discharge capacity of these subsequent cycles showed two plateaus for all samples. The high voltage plateau at 2.3 V vs Li/Li$^+$ has a length of 200−295 mAh/g$_S$, and the low voltage plateau at 2.0 V vs Li/Li$^+$ has a length between 858 and 1230 mAh/g$_S$ for all samples. Figure 2F displays the discharge capacity of AC1-S for cycles one to four, with values of 1237 mAh/g$_S$ to 945 mAh/g$_S$, and Figure 2G records 1119 mAh/g$_S$ to 859 mAh/g$_S$ for AC1−800-S for cycles one to four. The AC1−1000-S delivered a discharge capacity of 1228 mAh/g$_S$ to 971 mAh/g$_S$ in cycles one to four (Figure 2H).

The specific discharge capacity values of the first cycles for AC1-S, AC1−800-S, and AC1−1000-S were higher than those of the carbonate-based electrolyte but still lower than the theoretical capacity of sulfur. This is because the polysulfide species (Li_2S_n, $n \geq 4$) are highly soluble in ether-based electrolytes and do not form an insoluble layer with more stable ethers, thereby increasing the kinetic reactions due to solution-mediated processes and enabling higher utilization of active materials.[62] The increased dissolutions influence parasitic shuttling reactions. This mechanism is also observed in AC1-S, AC1−800-S, and AC1−1000-S (Figure 2F−H). In addition, the discharge length of the lower plateau was shorter than the charge (long upper voltage plateau) for cycles one to four for all samples (Figure 2F−H). It is reported that the dissolution of polysulfides in ether-based electrolytes can be reduced by cycling the cells at a higher cutoff potential range of 1.7 to 2.8 V vs Li/Li$^+$.[63] However, this technique reduces the cell potential, making the transition between Li_2S_2 and Li_2S more challenging and less complete.

Figure 3A,B presents the discharge and charge profiles of the fifth cycle for the carbonate-based and ether-based electrolytes at the cutoff potential of 1.0−3.0 V vs Li/Li$^+$ with 0.1C rate. The initial discharge capacity at 0.1C was 804 mAh/g$_S$ (AC1-S), 742 mAh/g$_S$ (AC1−800-S), and 818 mAh/g$_S$ (AC1−1000-S) for the carbonate-based electrolyte (Figure 3A). At the same time, the ether-based electrolyte had an initial discharge capacity of 539 mAh/g$_S$ (AC1-S), 603 mAh/g$_S$ (AC1−800-S), and 741 mAh/g$_S$ (AC1−1000-S), as shown in Figure 3B. AC1−1000-S exhibits flat discharge potential plateau features with a higher specific discharge capacity (818 mAh/g$_S$) than

https://doi.org/10.1021/acsaem.5c01629
ACS Appl. Energy Mater. 2025, 8, 12139−12156

Table 3. Comparison of Cathode Material, Electrolyte, and Electrochemical Performance for Li−S Batteries (n.a. Represents Not Applicable/Not Reported)[a]

sulfur cathode	electrolyte type/amount per mg_S	potential (V vs Li/Li^+)	initial capacity (mAh/g_S)/rate (C)	final capacity (mAh/g_S)/rate (C)	cycle number	sulfur content (mass %)	refs
AC1-S (AC/S)	1 M $LiPF_6$ in FEC/DMC (1:4 by volume)/40 μL	1−3	1106/0.05	536/0.1	100	52	this work
AC1−800-S (AC/S)	1 M $LiPF_6$ in FEC/DMC (1:4 by volume)/40 μL	1−3	1006/0.05	559/0.1	100	51	this work
AC1−1000-S (AC/S)	1 M $LiPF_6$ in FEC/DMC (1:4 by volume)/40 μL	1−3	1077/0.05	573/0.1	100	50	this work
AC1−1000−1C1.25S (AC/S)	1 M $LiPF_6$ in FEC/DMC (1:4 by volume)/40 μL	1−3	1336/0.05	584/0.1	50	56	this work
C/S-3 (AC/S)	1 M LiTFSI DOL/DME (1:1 by volume)/n.a.	1−3	1106/0.2	400/0.2	50	60	29
KJEC-600 (C/S: pristine)	1 M $LiPF_6$ in EC/DEC/EMC (1:1:1 by volume)/n.a.	1−3	940/0.1	∼100/0.1	100	67	35
KJEC-600 (C−S: alucone coated)	1 M $LiPF_6$ in EC/DEC/EMC (1:1:1 by volume)/n.a.	1−3	912/0.1	429/0.1	100	61	35
TiC-CDC-S_300	1 M $LiPF_6$ in EC/DMC (1:1 by volume)/30 μL	0.5−3	800/0.1	536/0.1	100	40	49
AC-RH/S2	1 M LiTFSI DOL/DME (1:1 in 0.1 M $LiNiO_3$)/20 μL	1.5−3	1102/0.1	335/0.2	100	42	67
glucosamine	1 M LiTFSI DOL/DME (1:1 in 0.1 M $LiNiO_3$)/60 μL	1.5−3	1194/0.1	505/0.1	100	50	68
S/OPNC-600 (AC/S)	1 M LiTFSI DOL/DME (1:1 in 1% $LiNiO_3$)/n.a.	1.7−3	921/0.2	489/0.2	300	54	70
S-G mixture (AC/S)	1 M LiTFSI DOL/DME (1:1 in 0.1 M $LiNiO_3$)/n.a.	1.5−3	1300/0.2	320/0.2	100	50	73
S/MC-50 (AC/S)	1 M $LiPF_6$ in PC/EC/DEC (1:4:5 by volume)/n.a.	1−3	1625/0.03	559/0.03	50	50	72
S-RGO	1 M $LiPF_6$ in EC/DMC/DEC (1:1:1 by volume)/n.a.	1−3	∼1000/0.02	∼500/0.02	120	32	74
SPAN-LSI	1 M $LiPF_6$ in EC/PC/DEC (1:1:3 by mass)/n.a.	1−3	965/0.05	∼500/0.5	100	42	69
KJ-EC600 (C−S)	1 M $LiPF_6$ in EC/DEC (1:1 by volume)/n.a.	1−3	∼1050/0.1	∼550/0.1	100	70	71
KJ-EC600 (C−S)	1 M $LiPF_6$ in EC/DEC (with 20 vol % FEC)/n.a.	1−3	∼1100/0.1	670/0.1	100	70	71

[a]The cycle number for the final capacity values of the compared studies was set to 100 cycles for comparison, unless otherwise indicated by the study; the reported final capacity value was displayed as shown in the column.

AC1-S (804 mAh/g_S) and AC1−800-S (742 mAh/g_S) for the carbonate-based electrolyte (Figure 3A). The performance improvement in AC1−1000-S was also observed for ether-based electrolytes (Figure 3B), indicating enhanced electrochemical performance with reduced polarization for both electrolytes. For AC1-S and AC1−800-S, the polarization was higher for both electrolytes (Figure 3A,B), which is associated with their limited porosity, which does not provide sufficient space for volume expansion. All cathodes were further investigated by electrochemical impedance measurements in both electrolyte systems. Supporting Information, Figure S4C−D present the Nyquist impedance plots for AC1-S, AC1−800-S, and AC1−1000-S in carbonate and ether-based electrolytes. The AC1−1000-S cell shows small charge transfer resistance (R_{ct}) in both electrolytes (Supporting Information, Figure S4C−D), indicating fast charge transfer kinetics for this sample.[20,64]

Further analysis of the cycling stability of AC1-S, AC1−800-S, and AC1−1000-S at 0.1C in both electrolytes is shown in Figure 3C−D. An improvement in cycling stability was observed for the carbonate-based electrolyte (Figure 3C), with discharge capacities of 540 mAh/g_S, 558 mAh/g_S and 598 mAh/g_S recorded after 80 cycles for AC1-S, AC1−800-S and AC1−1000-S compared to 338 mAh/g_S (AC1-S), 286 mAh/g_S (AC1−800-S), and 466 mAh/g_S (AC1−1000-S) for the ether-based electrolyte (Figure 3D). The cathodes exhibited a stable Coulombic efficiency of 99.73% (AC1-S), 99.94% (AC1−800-S) and 99.99% (AC1−1000-S) in carbonate-based electrolytes (Figure 3C) and unstable in ether-based electrolytes (Figure 3D) with 98−98.5% (AC1-S), 96.5−97.5% (AC1−800-S) and 98.5−99.5% (AC1−1000-S). The results are consistent with the observations in Figure 3A,B. The Coulombic efficiency below 99.9% in carbonate-based electrolytes is likely due to constant lithium stripping and parasitic reactions at the Li metal anode. In comparison, the Coulombic efficiency below 100% in ether-based electrolytes is associated with the loss of active material due to polysulfide dissolution.[65]

A considerable discharge capacity loss was observed during cycling (Figure 3D) for the ether-based electrolyte. The improvement in the cycling performance of the carbonate-based electrolyte (Figure 3C) is related to the addition of FEC additives to the electrolyte. The FEC helps stabilize the CEI in the cathode and the Li anode, enhancing fast Li-ion transport. Additionally, AC1−1000-S exhibited better cycling stability than AC1-S and AC1−800-S, which can be attributed to its porous structure (1.2 nm), involved in solid-state electrochemical conversion and providing room for volume expansion during the discharge and charge processes. The approximately 1 nm micropore carbon matrix is wide enough to accommodate S_8 molecules when properly aligned near the pore entrance.[66] The ether-based electrolyte's low performance may be related to its high polysulfide solubility, which

https://doi.org/10.1021/acsaem.5c01629
ACS Appl. Energy Mater. 2025, 8, 12139−12156

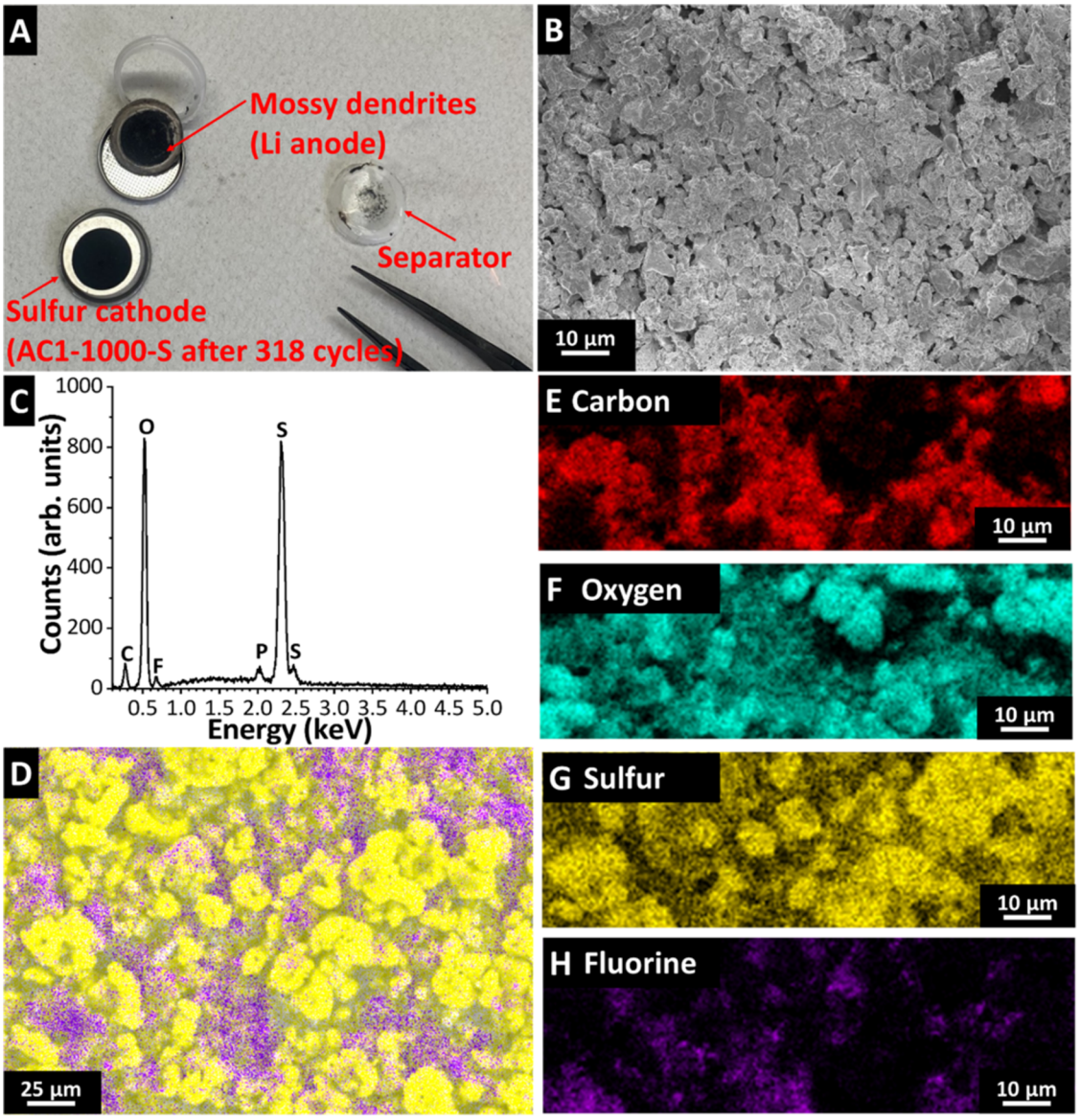

Figure 5. Post-mortem analysis: The disassembled AC1−1000-S cell after 318 cycles (A), scanning electron micrographs of the electrode (B), EDS elemental analysis showing the presence of C, O, S, and F (C), EDS mapping of the electrode showing an inhomogeneous distribution of fluorine after long cycles (D), and elemental mapping of different elements in the electrode structure (E−H).

enhances the shuttle effect. These results demonstrate that cathode materials display distinct reactions in various electrolytes.

Figure 4A shows the AC1-S, AC1−800-S, and AC1−1000-S cycling stability for up to 200 cycles. The 200 cycles were chosen to evaluate the behavior of these samples after long cycles and to highlight the significance of testing beyond 100 cycles. Despite the slight difference in mass % of sulfur (Table 2), all cathodes showed almost identical initial sulfur utilization using the carbonate-based electrolyte. AC1−1000-S showed a higher capacity in the first 100 cycles (Figure 4A), but the capacity slowly decreased in the subsequent cycles. To further elaborate on the impact of a higher specific pore volume, we increased the AC1−1000-S (1C:1S) sulfur loading to AC1−1000-S-1C:1.25S and AC1−1000-S-1C:1.5S (Section 3.3) and tested them with the carbonate-based electrolyte. As seen in Table 2, the AC1−1000-S samples are referred to as AC1−1000-S-50% (1C:1S), AC1−1000-S-56% (1C:1.25S), and AC1−1000-S-61% (1C:1.5S). The electrochemical measurements were carried out under identical conditions as before (C/20 in a potential range of 0.5−3.0 V vs Li/Li^+ for five formation cycles and C/10 in a voltage range of 1.0−3.0 V vs Li/Li^+ in the subsequent cycles).

Figure 4B shows an increase in initial discharge capacity to 1336 mAh/g_S and 1192 mAh/g_S for AC1−1000-S-56% and AC1−1000-S-61%, which is higher than 1077 mAh/g_S for AC1−1000-S-50%. The increase in the initial discharge capacity for AC1−1000-S-56% and AC1−1000-S-61% aligns with previous work and may be associated with improved charge transfer at higher sulfur loading.[44] Additionally, AC1−1000-S-56% exhibited a higher discharge capacity for up to 35 cycles, followed by a gradual decay in discharge capacity in subsequent cycles. The reason for this decay in comparison to AC1−1000-S-50% is that during the conversion reaction, the fraction of sulfur decreases with an increase in sulfur content, and this behavior is more pronounced in the sulfur cathode with AC1−1000-S-61% (Figure 4B), suggesting that there is an optimal C/S ratio based on the micropore structure.[28,29,44]

https://doi.org/10.1021/acsaem.5c01629
ACS Appl. Energy Mater. 2025, 8, 12139−12156

Table 4. Chemical Composition (atom %) Obtained from XPS Measurements of the AC1-S, AC1-800-S, and AC1-1000-S Cathodes and Anode in Carbonate-Based Electrolytes after the First Discharge (First Value) and 10th Discharge (Second Value)[a]

	cathode			anode		
element	AC1-S	AC1−800-S	AC1−1000-S	Li; AC1-S	Li; AC1−800-S	Li; AC1−1000-S
C	28/27	20/18	15/32	35/27	20/21	19/29
P	4/4	8/5	10/4	2.5/3	4/6	5/3
O	18/18	24/21	30/18	20/20	17/25	19/21
F	49/50	48/54	45/44	39/50	57/47	57/45
S	1/1	0/0	0/1	2.5/0	2/0	0/1
Ni	n.d/n.d	n.d/n.d	n.d/1	n.d/n.d	n.d/n.d	n.d/n.d
Li	n.d/n.d	n.d/2	n.d/n.d	n.d/n.d	n.d/n.d	n.d/n.d

[a]The n.d. stands for not detected within the detection limits of the method.

Furthermore, the AC1−1000-S-61% results indicated that some residual sulfur (Supporting Information, Figure S2H) is located outside the carbon matrix and/or at the pore entrance when compared to AC1−1000-S-56% (Supporting Information, Figure S2G). This increases the dissolution of polysulfides in the electrolyte and produces a parasitic side reaction between the polysulfide and carbonates, resulting in rapid capacity decay. This interpretation is in line with the TGA analysis (Supporting Information, Figure S3A), which indicated some fraction of surface sulfur particles, specifically for the AC1−1000-S-61%, whose complete evaporation occurred at a lower temperature compared to AC1−1000-S-50% and AC1−1000-S-56%. This indicates that sulfur outside the carbon matrix undergoes polysulfide shuttling, leading to high-capacity fading. We confirm that the inclusion of sulfur in the micropores is essential in reducing the shuttle effect mechanism, which contributes to high-capacity fading in Li−S batteries. The resulting electrochemical performance values, in particular after cycling, are competitive with the literature (Table 3).[29,35,49,67−74]

From the above context, we observed that the high capacity fading in the high sulfur loading cathode (AC1−1000-S-61%) is related to some sulfur particles outside the carbon matrix. We examined the relationship between sulfur loading and electrochemical performance to gain insight into the capacity fading rate. The capacity fading rate (f_c) was calculated from Figure 4B as follows[29]

$$f_c = \frac{C_1 - C_n}{n} \tag{2}$$

where C_1 and C_n represent the specific discharge capacities of the first and nth cycles, with n representing the number of cycles. Figure 4C shows the capacity fading rates of the cathode samples with different sulfur loading. The capacity fading rate was 8 mAh/g_S/cycle, 13 mAh/g_S/cycle, and 19 mAh/g_S/cycle for AC1−1000-S-50%, AC1−1000-S-56%, and AC1−1000-S-61%, respectively. We can observe that the fading rate increases as the sulfur content increases. This indicates that for AC1−1000-S-61% with a high rate of fading per cycle, the majority of the sulfur was located outside the carbon matrix after filling the pores, thereby increasing polysulfide dissolution and reducing reversibility. Therefore, cathode engineering should consider the available pore structure and the amount of sulfur that can be accommodated to reduce the excess sulfur dissolved in the electrolyte and increase the capacity fading.

To investigate whether the depletion of electrolytes causes capacity fading, we conducted an electrochemical analysis by adjusting the electrolyte volume for AC1−1000-S-56%. This analysis revealed an improvement in discharge capacities, sustaining up to 35 cycles (Figure 4B). The measurements were carried out to understand whether the decrease in cycling stability after 35 cycles was related only to the high sulfur loading and not to the amount of electrolyte used. Figure 4D displays the electrochemical measurement of AC1−1000-S-56% cells performed with different electrolyte amounts from 10 μL/mg_S to 50 μL/mg_S. The results show that reduced electrolyte does not correlate with higher sulfur loading. This is because the 40 μL/mg_S cell presented higher cycling stability compared to the 10 μL/mg_S, 20 μL/mg_S, and 30 μL/mg_S cells. Additionally, the cell with a higher electrolyte concentration (50 μL/mgS) displays significant capacity fading due to the increased dissolution of polysulfide. These results show that an optimal amount of electrolyte is required based on the cathode structure, which does not correlate with the higher sulfur loading.

3.5. Post-Mortem Analysis. To better understand the reduction in discharge capacity after 100 cycles for AC1−1000-S (Figure 4A), which exhibited improved cycling stability related to the pore structure, we performed a post-mortem analysis of the electrode after 318 cycles (Supporting Information, Figure S3D). The AC1−1000-S cell was discharged to a lower potential of 1 V vs Li/Li^+ and held for 2 h to ensure complete discharge, and was later disassembled. After opening the cell, we noticed that the mossy dendrites were lithium passivated due to FEC decomposition, as seen in Figure 5A. Additionally, the reactions between the electrolyte and polysulfide (after 318 cycles) may be related to the passivation of the lithium anode after prolonged cycling. Furthermore, as a part of this physical observation, we performed the SEM analysis on the AC1−1000-S electrode. Figure 5B shows a scanning electron micrograph of the electrode, displaying a stable structure without surface cracks, along with elemental distributions of C, O, F, and S (Figure 5C,D−H). The formation of the CEI/SEI layer with carbonate solvents was sustained for 100 cycles (Figure 4A) but seemingly consumed in subsequent cycles due to the significant volume change during lithium plating. This was confirmed by the EIS measurements performed at different cycling voltammograms, as shown in Supporting Information, Figure S4E−G, and further investigated using XPS.

We conducted a detailed analysis to investigate the effects of different electrolytes on the formation and evolution of the CEI and SEI after the first and 10th discharge cycles. This study aims to enhance our understanding of (a) the composition of the CEI/SEI layers, (b) their degradation

https://doi.org/10.1021/acsaem.5c01629
ACS Appl. Energy Mater. 2025, 8, 12139−12156

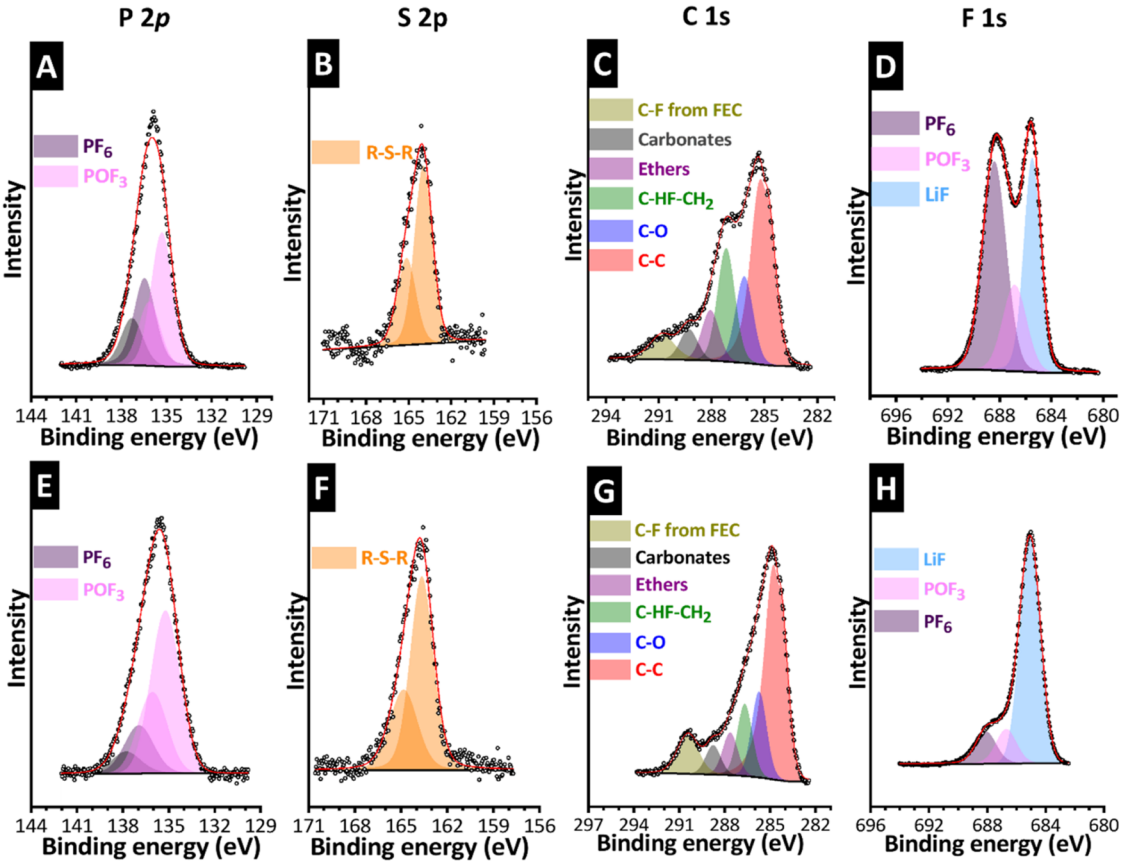

Figure 6. High-resolution X-ray photoelectron spectra of the AC1−1000-S cathode at the discharge state after 1st cycle (top; A−D) and 10th cycles (bottom; E−H) in carbonate-based electrolytes: P 2p (A, E), S 2p (B, F), C 1s (C, G) and F 1s (D, H). The circular dots represent experimental data, the red line is the composite spectrum, and the black line is the background used for peak fitting.

over cycles, and (c) the loss of active material. The analysis included extended spectra to determine the quantitative composition (Table 4 for carbonate-based electrolyte and Supporting Information, Table S2 for ether-based electrolyte), as well as high-resolution scans for the P 2p, S 2p, C 1s, N 1s, O 1s, and F 1s regions (Figures 6−7 for carbonate-based electrolyte and Supporting Information, Figures S6−S8 for ether-based electrolyte). Despite conducting high-resolution measurements on all samples, the results across the different cathodes (AC1-S, AC1−800-S, and AC1−1000-S) and their respective anodes were broadly similar (Supporting Information, Figure S5A,B for the ether-based electrolyte and Supporting Information, Figure S5C−D for the carbonate-based electrolyte).

In this regard, we focused our analysis on the AC1−1000-S cathode and anode surfaces to gain deeper insights, as this cathode showed better stability compared to others. Elemental composition analysis (Supporting Information, Table S2 for ether-based electrolyte) revealed that the surfaces of the three cathodes displayed similar atomic compositions, primarily consisting of fluorine (40 atom %), along with carbon, oxygen, and sulfur, with nitrogen being the least abundant at around 5 atom %. Nitrogen and fluorine primarily originate from the LiTFSI and $LiNO_3$ salts. No significant differences were observed between the first and 10th discharge cycles, indicating that the composition of the CEI remained stable throughout these cycles.

For the ether-based electrolyte, high-resolution C 1s spectra (Supporting Information, Figure S6A,E) showed no sp^2 carbon signal, suggesting that the CEI thickness exceeds the XPS probing depth of approximately 5 to 10 nm.[75,76] The C 1s spectra revealed a peak corresponding to sp^3 C−H bonds at 285.3 eV, associated with electrolyte solvent molecules. Additionally, five other signals were detected: C−O−C bonds (286.1 eV), C−S bonds (287.3 eV, from the LiTFSI salt), ethers (288.7 eV), carbonates (289.9 eV), and CF_3 (293.4 eV, also from LiTFSI). The presence of carbonates is likely due to electrolyte solvent decomposition, as proposed in the literature.[60] The dominant signal in the C 1s spectra comes from the LiTFSI salt, indicating a substantial presence of salt on the cathode surface, corroborated by the S 2p at 169.8 eV (Supporting Information, Figure S6B,F), N 1s at 400.1 eV (Supporting Information, Figure S6C,G), and F 1s at 689.2 eV signals (Supporting Information, Figure S6D,H).[77] Additionally, the S 2p spectra (Supporting Information, Figure S6B,F) revealed Li_2S at 160.53 eV, alongside polysulfides at 162.0 eV (terminal) and 163.6 eV (bridging),[78] and SO_x species at 167.6 eV. The bridging-to-terminal ratio is almost 1, corresponding to the mean Li_2S_4 polysulfide. Between the first and 10th cycles, the number of polysulfides and SO_x species increased, likely due to the shuttle effect, in which more polysulfides dissolved into the electrolyte and contributed to irreversible side reactions.[79] The N 1s spectra (Supporting Information, Figure S6C,G) also indicated the presence of Li_3N at 397.9 eV, likely originating from $LiNO_3$ decomposition.[80] Li_3N is a well-known ionic conductor, often used for protecting Li metal.[80,81]

The elemental composition of the lithium metal anode (Supporting Information, Table S2 for ether-based electrolyte)

https://doi.org/10.1021/acsaem.5c01629
ACS Appl. Energy Mater. 2025, 8, 12139−12156

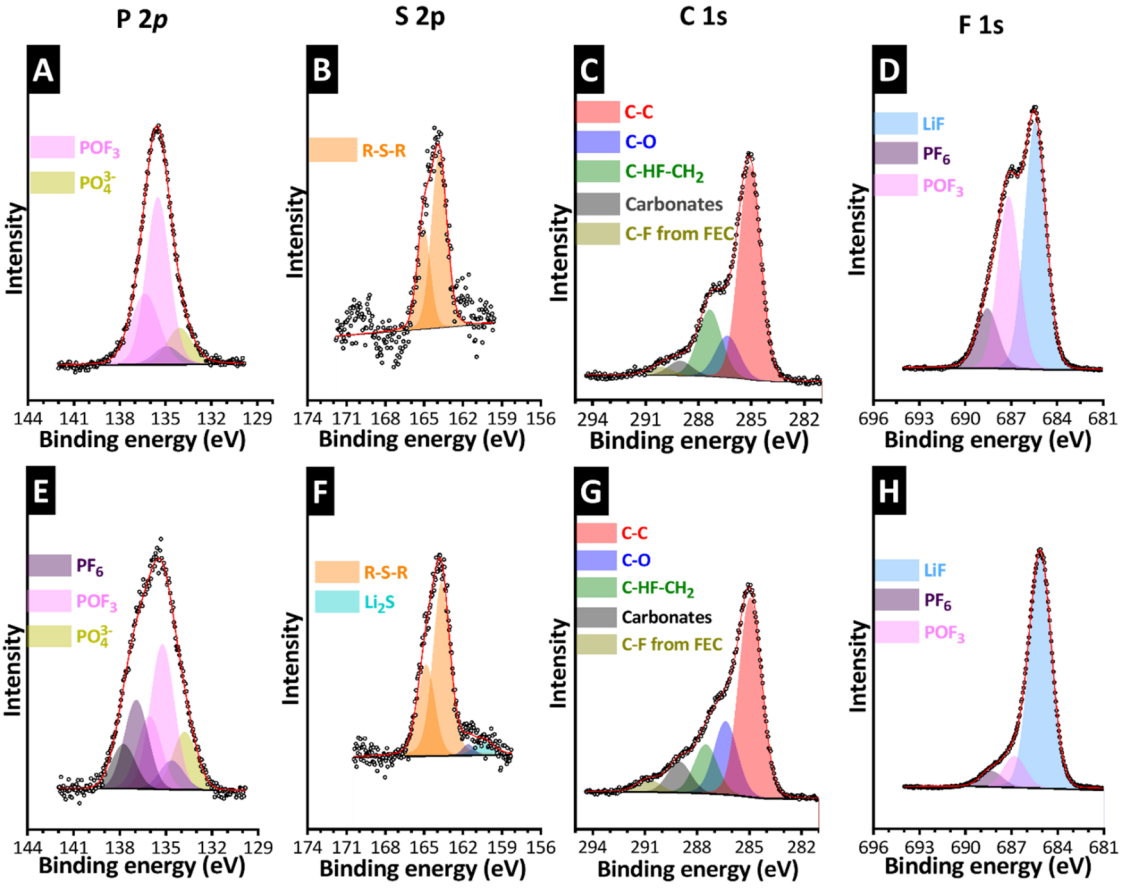

Figure 7. High-resolution X-ray photoelectron spectra of the AC1−1000-S anode at the discharge state after 1st cycle (top; A−D) and 10th cycles (bottom; E−H) in carbonate-based electrolytes: P 2p (A, E), S 2p (B, F), C 1s (C, G), and F 1s (D, H). The circular dots represent experimental data, the red line is the composite spectrum, and the black line is the background.

reveals an increase in carbon and oxygen content from the first to the 10th cycle, accompanied by a reduction in fluorine. At the same time, sulfur and nitrogen levels remained relatively similar. To better understand these changes, high-resolution spectra were inspected. Figure S7, Supporting Information presents the high-resolution spectra for S 2p (Supporting Information, Figure S7A,D), C 1s (Supporting Information, Figure S7B,E), O 1s (Supporting Information, Figure S7C,F), and the deconvolutions show the same contributions as observed on the cathode surface, with two notable exceptions: after ten cycles, the C 1s spectra indicated the presence of sp^2 carbon (Supporting Information, Figure S7B,E) and the O 1s spectrum show a new peak at 531.2 eV (Supporting Information, Figure S7C,F). The decomposition of DOL can explain the appearance of these two contributions during the formation of the SEI on the lithium metal anode surface. The cyclic ether structure of DOL can undergo ring-opening polymerization and cross-linking in reactive environments, such as the lithium anode, leading to the formation of partially conjugated polymers that contribute to the observed sp^2 carbon signal.[60,82] This is confirmed by the O 1s spectra, where a new peak at 531.2 eV can be assigned to C═O carbonyl groups in conjugated polymers formed from ring-opening reactions.[60] The N 1s (Supporting Information, Figure S8A,C) and F 1s (Supporting Information, Figure S8B,D) spectra show the same contribution observed on the cathode side.

For the carbonate-based electrolyte, survey analysis of the cathode and anode revealed minimal or no sulfur on the electrode surfaces (Table 4). This result is expected, as the shuttle effect is typically suppressed in microporous carbons with a carbonate-based electrolyte. Furthermore, this suggests that the CEI largely covers the surface of the cathode, as significant sulfur presence would otherwise be detected in the survey spectra. Small amounts of sulfur were observed on the lithium metal anode, likely due to dissolved sulfur species, although the levels remained below 2.5 atom %. The CEI and SEI are mostly composed of fluorine (49/50 atom %), carbon (28/27 atom %), and oxygen (18/18 atom %), with phosphorus at approximately 5 atom %.

High-resolution fluorine spectra from both anode and cathode reveal the presence of three peaks, indicating the formation of LiF (approximately 685.2 eV), PF_6 anion (around 688.2 eV), and another signal at 686.8 eV (Figures 6D,H and 7D,H for carbonate-based electrolyte). This latter contribution is attributed to the electrochemical decomposition of the PF_6 anion into POF_3^- on the cathode and anode surfaces.[77] This observation is supported by the P 2p spectra (Figures 6A,E and 7A,E for carbonate-based electrolyte), which show two contributions at 135.3 eV (for POF_3^-) and 136.4 eV (for PF_6^-). Additionally, on the anode surface, POF_3^- can further decompose into PO_4^{3-}, contributing to another feature in the P 2p spectra at 134.6 eV (Figure 7D,H for carbonate-based electrolyte). The S 2p spectra from both the cathode and anode reveal a prominent peak at 163.6 eV across the first and

https://doi.org/10.1021/acsaem.5c01629
ACS Appl. Energy Mater. 2025, 8, 12139−12156

10th cycles, which may be assigned to R-S-R sulfide species formed after nucleophilic reactions between the electrolyte and polysulfides (Figures 6B,F and 7B,F for carbonate-based electrolyte).[83] This finding explains the cause of capacity fading and the observations made during the physical inspection of the lithium metal anode after cycling (Figure 5A).

The C 1s spectrum for carbonate-based electrolyte was deconvoluted into six distinct contributions (Figures 6C,G and 7C,G). The first contribution, at 284.9 eV, corresponds to sp^2 and sp^3 C−C bonds. At 286.4 eV, there is a contribution to C−O bonds, followed by the signal at 287.3 eV assigned to C−HF−CH_2 species from FEC decomposition.[84] At 288.7 eV, there is the contribution from ether species (only for the cathode surface), and finally, the peak at 289.4 eV is assigned to the FEC and DMC carbonate solvents.[83] Lastly, at 290.5 eV, we see the C−F bonds from FEC. The ether signal likely originates from the decomposition of DMC and FEC. Notably, the same reaction mechanism that produces R−S−R sulfide species may also lead to the formation of ethers.[85] The ether signal is observed solely on the cathode surface, suggesting that polysulfides, once formed, immediately react with the electrolyte. This reaction allows sulfide species to migrate toward the anode side, which could further reduce Li_2S (Figure 7F). These findings indicate that the CEI and SEI layers on the cathode and anode share a similar chemical composition in carbonate-based electrolytes. These layers are primarily composed of LiF and $LiPOF_3$, and in the anode case, Li_3PO_4 is formed from the decomposition of FEC and $LiPF_6$. The presence of these stable inorganic compounds may contribute to the formation of a robust SEI and CEI, potentially enhancing mechanical stability[86] and ionic conductivity.[87,88] Together, these components protect against unwanted side reactions, thereby improving the overall stability and performance of the battery.

4. CONCLUSIONS

We have successfully produced activated carbons (AC1−800 and AC1−1000) of varying pore sizes by CO_2 activation, infiltrated with the same C/S ratios, and tested them as cathodes in carbonate-based and ether-based electrolytes to examine the influence of the CEI/SEI layer on the cycling performance. The activation process was designed to enhance pore volume, thereby facilitating lithium-ion transport and enabling sulfur confinement within the micropores, which helps suppress polysulfide shuttling and improves the cycling stability of Li−S batteries. The AC1−1000-S, with 50 mass % S and the highest porosity, showed maximum sulfur utilization and good cycling stability in carbonated-based electrolytes, which have been reported to be incompatible with C/S cathodes without microporosity. The *ex situ* XPS analysis confirmed that the CEI and SEI formed at the cathode and anode, respectively, share a similar chemical composition, which improves mechanical stability and ionic conductivity, which affects battery performance. The AC1−1000-S was further infiltrated with different C/S ratios, and the maximum sulfur attained was 61 mass %. Based on our findings, cathode engineering should prioritize optimizing the pore structure and capacity to effectively accommodate sulfur. These results contribute to the Li−S battery scientific community by highlighting the importance of cathode engineering with optimized pore structures in balancing sulfur accommodation, reducing polysulfide shuttling, and mitigating capacity degradation using carbonate-based electrolytes. The study also highlights the practical implications of the solubility of polysulfides, which controls sulfur utilization.

■ ASSOCIATED CONTENT

Data Availability Statement

The data that support the findings of this study are available from the corresponding author upon reasonable request.

Supporting Information

The Supporting Information is available free of charge at https://pubs.acs.org/doi/10.1021/acsaem.5c01629.

Comparisons of the electrochemical performances of AC1-S and AC2-S; SEM images; TGA analysis of AC1−1000−1C1S (50%), AC1−1000−1C1.25S (56%), and AC1−1000−1C1.5S (61%) (A); XRD analysis of AC1−1000 with higher sulfur loading; WAXS analysis of AC1, AC1−800, and AC1−1000, as well as the sulfur infiltrated samples AC1-S, AC1−800-S, AC1−1000-S, and AC1−1000−1C1.25S; cycling stability and Coulombic efficiency of AC1-S, AC1−800-S, and AC1−1000-S in a carbonate-based electrolyte until the cell was stopped (D); cyclic voltammograms and EIS results of AC1-S, AC1−800-S, and AC1−1000-S in carbonate-based electrolyte, and ether-based electrolyte; High-resolution C 1s XPS of AC1-S, AC1−800-S, and AC1−1000-S for an ether-based cathode or anode and a carbonate-based cathode or anode; high-resolution XPS of AC1−1000-S cathode at the discharge state after 1st and 10th cycles in ether-based electrolyte; High-resolution XPS of the AC1−1000-S anode at the discharge state after 1st and 10th cycles in ether-based electrolyte; Raman spectra of the D- and G-bands fitted position using the Voigt function; and atomic concentration (atom %) obtained from XPS measurements of the AC1-S, AC1−800-S, and AC1−1000-S cathodes and anode in ether-based electrolytes after the 1st discharge (first value) and 10th discharge (second value) (PDF)

■ AUTHOR INFORMATION

Corresponding Author

Volker Presser − *INM—Leibniz Institute for New Materials, 66123 Saarbrücken, Germany; Department of Materials Science and Engineering, Saarland University, 66123 Saarbrücken, Germany; saarene—Saarland Center for Energy Materials and Sustainability, 66123 Saarbrücken, Germany;* orcid.org/0000-0003-2181-0590; Email: volker.presser@leibniz-inm.de

Authors

Delvina Japhet Tarimo − *INM—Leibniz Institute for New Materials, 66123 Saarbrücken, Germany*

Francisco J. García-Soriano − *National Institute of Chemistry, 1001 Ljubljana, Slovenia;* orcid.org/0000-0001-8805-5935

Alen Vizintin − *National Institute of Chemistry, 1001 Ljubljana, Slovenia;* orcid.org/0000-0003-1876-1396

Christian Prehal − *University of Salzburg, Department of Chemistry and Physics of Materials, 5020 Salzburg, Austria;* orcid.org/0000-0003-0654-0940

Complete contact information is available at: https://pubs.acs.org/10.1021/acsaem.5c01629

https://doi.org/10.1021/acsaem.5c01629
ACS Appl. Energy Mater. 2025, 8, 12139−12156

Author Contributions

D.J.T.: Conceptualization, Methodology, Investigation, Data curation, Validation, Visualization, Writing—Original Draft, Review and Editing. F.J.G.S.: Conceptualization, Investigation, Data curation, Validation, Review and Editing. A.V.: Conceptualization, Investigation, Data curation, Validation, Review and Editing. C.P.: Investigation, Data curation, Validation, Review and Editing. V.P.: Conceptualization, Validation, Data curation, Funding Acquisition, Review and Editing.

Notes

The authors declare no competing financial interest.

■ ACKNOWLEDGMENTS

The INM authors acknowledge the German Federal Ministry for Research and Education (BMBF), and the NIC authors acknowledge the Slovenian Ministry of Higher Education, Science and Innovation (MVZI) for funding the joint M-ERA.NET ALISA project (PR-457221). The authors thank Andrea Jung (INM) for performing the CHNS-O analysis and Mingren Liu (INM) for helpful discussions and insightful revision. D.J.T. acknowledges funding from the Alexander von Humboldt Foundation. A.V. acknowledges the financial support from the Slovenian Research and Innovation Agency (ARIS) under the research core program P2-0423.

■ REFERENCES

(1) Jiang, T.; Shen, D.; Zhang, Z.; Liu, H.; Zhao, G.; Wang, Y.; Tan, S.; Luo, R.; Chen, W. Battery technologies for grid-scale energy storage. *Nat. Rev. Clean Technol.* **2025**, *1* (7), 474−492.

(2) Purbayanto, M. A. K.; Presser, V.; Skarżyński, K.; Słoma, M.; Naguib, M.; Jastrzębska, A. M. MXenes: Multifunctional Materials for the Smart Cities of Tomorrow. *Adv. Funct. Mater.* **2025**, *35* (10), No. 2409953.

(3) Etacheri, V.; Marom, R.; Elazari, R.; Salitra, G.; Aurbach, D. Challenges in the development of advanced Li-ion batteries: a review. *Energy Environ. Sci.* **2011**, *4* (9), 3243−3262 10.1039/C1EE01598B.

(4) Edge, J. S.; O'Kane, S.; Prosser, R.; Kirkaldy, N. D.; Patel, A. N.; Hales, A.; Ghosh, A.; Ai, W.; Chen, J.; Yang, J.; et al. Lithium ion battery degradation: what you need to know. *Phys. Chem. Chem. Phys.* **2021**, *23* (14), 8200−8221.

(5) Fang, R.; Zhao, S.; Sun, Z.; Wang, D. W.; Cheng, H. M.; Li, F. More reliable lithium-sulfur batteries: status, solutions and prospects. *Adv. Mater.* **2017**, *29* (48), No. 1606823.

(6) Arnold, S.; Gentile, A.; Li, Y.; Wang, Q.; Marchionna, S.; Ruffo, R.; Presser, V. Design of high-performance antimony/MXene hybrid electrodes for sodium-ion batteries. *J. Mater. Chem. A* **2022**, *10* (19), 10569−10585.

(7) Breitsprecher, K.; Janssen, M.; Srimuk, P.; Mehdi, B. L.; Presser, V.; Holm, C.; Kondrat, S. How to speed up ion transport in nanopores. *Nat. Commun.* **2020**, *11* (1), No. 6085.

(8) Seh, Z. W.; Sun, Y.; Zhang, Q.; Cui, Y. Designing high-energy lithium-sulfur batteries. *Chem. Soc. Rev.* **2016**, *45* (20), 5605−5634.

(9) Liu, T.; Hu, H.; Ding, X.; Yuan, H.; Jin, C.; Nai, J.; Liu, Y.; Wang, Y.; Wan, Y.; Tao, X. 12 years roadmap of the sulfur cathode for lithium sulfur batteries (2009−2020). *Energy Storage Mater.* **2020**, *30*, 346−366.

(10) Liu, J.; Bao, Z.; Cui, Y.; Dufek, E. J.; Goodenough, J. B.; Khalifah, P.; Li, Q.; Liaw, B. Y.; Liu, P.; Manthiram, A.; et al. Pathways for practical high-energy long-cycling lithium metal batteries. *Nat. Energy* **2019**, *4* (3), 180−186.

(11) Kim, J. T.; Su, H.; Zhong, Y.; Wang, C.; Wu, H.; Zhao, D.; Wang, C.; Sun, X.; Li, Y. All-solid-state lithium-sulfur batteries through a reaction engineering lens. *Nat. Chem. Eng.* **2024**, *1* (6), 400−410.

(12) Yari, S.; Reis, A. C.; Pang, Q.; Safari, M. Performance benchmarking and analysis of lithium-sulfur batteries for next-generation cell design. *Nat. Commun.* **2025**, *16* (1), No. 5473.

(13) Zhou, G.; Chen, H.; Cui, Y. Formulating energy density for designing practical lithium-sulfur batteries. *Nat. Energy* **2022**, *7* (4), 312−319.

(14) Zhang, B.; Qin, X.; Li, G.; Gao, X. Enhancement of long stability of sulfur cathode by encapsulating sulfur into micropores of carbon spheres. *Energy Environ. Sci.* **2010**, *3* (10), 1531−1537.

(15) Choudhury, S.; Srimuk, P.; Raju, K.; Tolosa, A.; Fleischmann, S.; Zeiger, M.; Ozoemena, K. I.; Borchardt, L.; Presser, V. Carbon onion/sulfur hybrid cathodes via inverse vulcanization for lithium-sulfur batteries. *Sustainable Energy Fuels* **2018**, *2* (1), 133−146 10.1039/C7SE00452D.

(16) Pang, Q.; Liang, X.; Kwok, C. Y.; Nazar, L. F. Advances in lithium-sulfur batteries based on multifunctional cathodes and electrolytes. *Nat. Energy* **2016**, *1* (9), No. 16132.

(17) Long, X.; Luo, Z.-H.; Zhou, W.-H.; Zhu, S.-K.; Song, Y.; Li, H.; Geng, C.-N.; Shi, B.; Han, Z.-Y.; Zhou, G.-M.; et al. Two-dimensional montmorillonite-based heterostructure for high-rate and long-life lithium-sulfur batteries. *Energy Storage Mater.* **2022**, *52*, 120−129.

(18) Tarimo, D. J.; Oyedotun, K. O.; Mirghni, A. A.; Sylla, N. F.; Manyala, N. High energy and excellent stability asymmetric supercapacitor derived from sulphur-reduced graphene oxide/manganese dioxide composite and activated carbon from peanut shell. *Electrochim. Acta* **2020**, *353*, No. 136498.

(19) Bai, Y.; Li, T.; Wang, Y.; Jin, H.; Wang, K.; Xu, H. Novel construction of nanostructured carbon materials as sulfur hosts for advanced lithium-sulfur batteries. *Int. J. Energy Res.* **2020**, *44* (1), 70−91.

(20) Kang, N.; Lin, Y.; Yang, L.; Lu, D.; Xiao, J.; Qi, Y.; Cai, M. Cathode porosity is a missing key parameter to optimize lithium-sulfur battery energy density. *Nat. Commun.* **2019**, *10* (1), No. 4597.

(21) Rouquerol, J.; Avnir, D.; Fairbridge, C. W.; Everett, D. H.; Haynes, J.; Pernicone, N.; Ramsay, J. D.; Sing, K. S. W.; Unger, K. K. Recommendations for the characterization of porous solids (technical report). *Pure Appl. Chem.* **1994**, *66* (8), 1739−1758.

(22) Evers, S.; Nazar, L. F. New approaches for high energy density lithium-sulfur battery cathodes. *Acc. Chem. Res.* **2013**, *46* (5), 1135−1143.

(23) Wang, Y.; Indubala, E.; Ma, C.; Zhang, C.; Li, C.; Zhang, W.; Chen, Y.; Zhao, Y.; Xiao, L.; Lv, B.; et al. Nitrogen doped three-dimensionally interconnected macroporous/mesoporous carbon nanofibers as free-standing electrode for room temperature sodium sulfur batteries. *Diamond Relat. Mater.* **2025**, *152*, No. 111997.

(24) Nightingale, E. R. Phenomenological theory of ion solvation. Effective radii of hydrated ions. *J. Phys. Chem. A* **1959**, *63* (9), 1381−1387.

(25) Li, X.; Cao, Y.; Qi, W.; Saraf, L. V.; Xiao, J.; Nie, Z.; Mietek, J.; Zhang, J.-G.; Schwenzer, B.; Liu, J. Optimization of mesoporous carbon structures for lithium-sulfur battery applications. *J. Mater. Chem.* **2011**, *21* (41), 16603−16610.

(26) Markevich, E.; Salitra, G.; Talyosef, Y.; Chesneau, F.; Aurbach, D. On the mechanism of quasi-solid-state lithiation of sulfur encapsulated in microporous carbons: is the existence of small sulfur molecules necessary? *J. Electrochem. Soc.* **2017**, *164* (1), No. A6244.

(27) He, G.; Ji, X.; Nazar, L. High "C" rate Li-S cathodes: sulfur imbibed bimodal porous carbons. *Energy Environ. Sci.* **2011**, *4* (8), 2878−2883.

(28) Fu, Y.; Singh, R. K.; Feng, S.; Liu, J.; Xiao, J.; Bao, J.; Xu, Z.; Lu, D. Understanding of low-porosity sulfur electrode for high-energy lithium-sulfur batteries. *Adv. Energy Mater.* **2023**, *13* (13), No. 2203386.

(29) Li, D.; Han, F.; Wang, S.; Cheng, F.; Sun, Q.; Li, W.-C. High sulfur loading cathodes fabricated using peapodlike, large pore volume mesoporous carbon for lithium-sulfur battery. *ACS Appl. Mater. Interfaces* **2013**, *5* (6), 2208−2213.

https://doi.org/10.1021/acsaem.5c01629
ACS Appl. Energy Mater. 2025, 8, 12139−12156

(30) Liu, Y.; Lin, D.; Liang, Z.; Zhao, J.; Yan, K.; Cui, Y. Lithium-coated polymeric matrix as a minimum volume-change and dendrite-free lithium metal anode. *Nat. Commun.* **2016**, *7* (1), No. 10992.
(31) Borchardt, L.; Oschatz, M.; Kaskel, S. Carbon materials for lithium sulfur batteries - ten critical questions. *Chem. - Eur. J.* **2016**, *22* (22), 7324−7351.
(32) Hou, L. P.; Li, Y.; Li, Z.; Zhang, Q. K.; Li, B. Q.; Bi, C. X.; Chen, Z. X.; Su, L. L.; Huang, J. Q.; Wen, R.; et al. Electrolyte design for improving mechanical stability of solid electrolyte interphase in lithium-sulfur batteries. *Angew. Chem., Int. Ed.* **2023**, *62* (32), No. e202305466.
(33) Zhang, S.; Ueno, K.; Dokko, K.; Watanabe, M. Recent advances in electrolytes for lithium-sulfur batteries. *Adv. Energy Mater.* **2015**, *5* (16), No. 1500117.
(34) Zhang, S. S. Effect of discharge cutoff voltage on reversibility of lithium/sulfur batteries with LiNO3-contained electrolyte. *J. Electrochem. Soc.* **2012**, *159* (7), No. A920.
(35) Li, X.; Lushington, A.; Sun, Q.; Xiao, W.; Liu, J.; Wang, B.; Ye, Y.; Nie, K.; Hu, Y.; Xiao, Q.; et al. Safe and durable high-temperature lithium-sulfur batteries via molecular layer deposited coating. *Nano Lett.* **2016**, *16* (6), 3545−3549.
(36) Aurbach, D.; Talyosef, Y.; Markovsky, B.; Markevich, E.; Zinigrad, E.; Asraf, L.; Gnanaraj, J. S.; Kim, H.-J. Design of electrolyte solutions for Li and Li-ion batteries: a review. *Electrochim. Acta* **2004**, *50* (2−3), 247−254.
(37) Zhang, S. S. Liquid electrolyte lithium/sulfur battery: Fundamental chemistry, problems, and solutions. *J. Power Sources* **2013**, *231*, 153−162.
(38) Yin, Y. X.; Xin, S.; Guo, Y. G.; Wan, L. J. Lithium-sulfur batteries: electrochemistry, materials, and prospects. *Angew. Chem., Int. Ed.* **2013**, *52* (50), 13186−13200.
(39) Urbonaite, S.; Poux, T.; Novák, P. Progress towards commercially viable Li-S battery cells. *Adv. Energy Mater.* **2015**, *5* (16), No. 1500118.
(40) Zhang, S. S.; Tran, D. T. A proof-of-concept lithium/sulfur liquid battery with exceptionally high capacity density. *J. Power Sources* **2012**, *211*, 169−172.
(41) Ding, N.; Chien, S. W.; Hor, T. A.; Liu, Z.; Zong, Y. Key parameters in design of lithium sulfur batteries. *J. Power Sources* **2014**, *269*, 111−116.
(42) Dörfler, S.; Althues, H.; Härtel, P.; Abendroth, T.; Schumm, B.; Kaskel, S. Challenges and key parameters of lithium-sulfur batteries on pouch cell level. *Joule* **2020**, *4* (3), 539−554.
(43) Zhou, L.; Danilov, D. L.; Qiao, F.; Wang, J.; Li, H.; Eichel, R. A.; Notten, P. H. Sulfur reduction reaction in lithium-sulfur batteries: mechanisms, catalysts, and characterization. *Adv. Energy Mater.* **2022**, *12* (44), No. 2202094.
(44) Gungor, A. S.; von Mentlen, J.-M.; Ruthes, J. G.; García-Soriano, F. J.; Talian, S. D.; Presser, V.; Porcar, L.; Vizintin, A.; Wood, V.; Prehal, C. Understanding rate and capacity limitations in Li-S batteries based on solid-state sulfur conversion in confinement. *ACS Appl. Mater. Interfaces* **2024**, *16* (49), 67651−67661.
(45) Para, M. L.; Calderón, C. A.; Talian, S. D.; Fischer, F.; Luque, G. L.; Barraco, D. E.; Leiva, E. P.; Dominko, R. Extending the conversion rate of sulfur infiltrated into microporous carbon in carbonate electrolytes. *Batteries Supercaps* **2022**, *5* (5), No. e202100374.
(46) Li, Z.; Guo, D.; Liu, Y.; Wang, H.; Wang, L. Recent advances and challenges in biomass-derived porous carbon nanomaterials for supercapacitors. *Chem. Eng. J.* **2020**, *397*, No. 125418.
(47) Tarimo, D. J.; Mirghni, A. A.; Oyedotun, K. O.; Rutavi, G.; Kitenge, V. N.; Manyala, N. Recycling of biomass wastes from amarula husk by a modified facile economical water salt method for high energy density ultracapacitor application. *J. Energy Storage* **2022**, *53*, No. 105166.
(48) Choudhury, S.; Krüner, B.; Massuti-Ballester, P.; Tolosa, A.; Prehal, C.; Grobelsek, I.; Paris, O.; Borchardt, L.; Presser, V. Microporous novolac-derived carbon beads/sulfur hybrid cathode for lithium-sulfur batteries. *J. Power Sources* **2017**, *357*, 198−208.
(49) Kensy, C.; Leistenschneider, D.; Wang, S.; Tanaka, H.; Dörfler, S.; Kaneko, K.; Kaskel, S. The role of carbon electrodes pore size distribution on the formation of the cathode-electrolyte interphase in lithium-sulfur batteries. *Batteries Supercaps* **2021**, *4* (4), 612−622.
(50) Sadezky, A.; Muckenhuber, H.; Grothe, H.; Niessner, R.; Pöschl, U. Raman microspectroscopy of soot and related carbonaceous materials: Spectral analysis and structural information. *Carbon* **2005**, *43* (8), 1731−1742.
(51) Ferrari, A. C. Raman spectroscopy of graphene and graphite: Disorder, electron-phonon coupling, doping and nonadiabatic effects. *Solid State Commun.* **2007**, *143* (1−2), 47−57.
(52) Oschatz, M.; Pre, P.; Dörfler, S.; Nickel, W.; Beaunier, P.; Rouzaud, J.-N.; Fischer, C.; Brunner, E.; Kaskel, S. Nanostructure characterization of carbide-derived carbons by morphological analysis of transmission electron microscopy images combined with physisorption and Raman spectroscopy. *Carbon* **2016**, *105*, 314−322.
(53) Howe, J. Y.; Rawn, C. J.; Jones, L.; Ow, H. Improved crystallographic data for graphite. *Powder Diffr.* **2003**, *18* (2), 150−154.
(54) Barczak, M.; Florent, M.; Bhalekar, S. S.; Kaneko, K.; Messinger, R. J.; Bandosz, T. J. Sulfur-tuned advanced carbons of novel properties and scalable productivity. *Adv. Funct. Mater.* **2024**, *34* (7), No. 2310398.
(55) Helen, M.; Diemant, T.; Schindler, S.; Behm, R. J. r.; Danzer, M.; Kaiser, U.; Fichtner, M.; Anji Reddy, M. Insight into sulfur confined in ultramicroporous carbon. *ACS Omega* **2018**, *3* (9), 11290−11299.
(56) Xu, Z.; Wang, J.; Yang, J.; Miao, X.; Chen, R.; Qian, J.; Miao, R. Enhanced performance of a lithium-sulfur battery using a carbonate-based electrolyte. *Angew. Chem., Int. Ed.* **2016**, *55* (35), 10372−10375.
(57) Xu, Y.; Wen, Y.; Zhu, Y.; Gaskell, K.; Cychosz, K. A.; Eichhorn, B.; Xu, K.; Wang, C. Confined sulfur in microporous carbon renders superior cycling stability in Li/S batteries. *Adv. Funct. Mater.* **2015**, *25* (27), 4312−4320.
(58) Dominko, R.; Vizintin, A.; Aquilanti, G.; Stievano, L.; Helen, M. J.; Munnangi, A. R.; Fichtner, M.; Arcon, I. Polysulfides formation in different electrolytes from the perspective of X-ray absorption spectroscopy. *J. Electrochem. Soc.* **2018**, *165* (1), No. A5014.
(59) Pai, R.; Singh, A.; Tang, M. H.; Kalra, V. Stabilization of gamma sulfur at room temperature to enable the use of carbonate electrolyte in Li-S batteries. *Commun. Chem.* **2022**, *5* (1), No. 17.
(60) Lodovico, L.; Varzi, A.; Passerini, S. Radical decomposition of ether-based electrolytes for Li-S batteries. *J. Electrochem. Soc.* **2017**, *164* (9), No. A1812.
(61) Barghamadi, M.; Best, A. S.; Bhatt, A. I.; Hollenkamp, A. F.; Mahon, P. J.; Musameh, M.; Rüther, T. Effect of $LiNO_3$ additive and pyrrolidinium ionic liquid on the solid electrolyte interphase in the lithium-sulfur battery. *J. Power Sources* **2015**, *295*, 212−220.
(62) Zhu, W.; Paolella, A.; Kim, C.-S.; Liu, D.; Feng, Z.; Gagnon, C.; Trottier, J.; Vijh, A.; Guerfi, A.; Mauger, A.; et al. Investigation of the reaction mechanism of lithium sulfur batteries in different electrolyte systems by in situ Raman spectroscopy and in situ X-ray diffraction. *Sustainable Energy Fuels* **2017**, *1* (4), 737−747.
(63) Zhang, S. S. Role of $LiNO_3$ in rechargeable lithium/sulfur battery. *Electrochim. Acta* **2012**, *70*, 344−348.
(64) Yuan, L.; Qiu, X.; Chen, L.; Zhu, W. New insight into the discharge process of sulfur cathode by electrochemical impedance spectroscopy. *J. Power Sources* **2009**, *189* (1), 127−132.
(65) García-Soriano, F. J.; Cometto, F.; Raviolo, S.; Slosar, T.; Tchernychova, E.; Genorio, B.; Dominko, R.; Bracamonte, M. V.; Vizintin, A. Biocarbon from olive pomace residue as a sulfur host for carbonate-based lithium-sulfur batteries. *Commun. Mater.* **2025**, *6* (1), No. 122.
(66) Steudel, R. *Elemental Sulfur and Sulfur-Rich Compounds II*; Springer, 2003.
(67) Vu, D.-L.; Seo, J.-S.; Lee, H.-Y.; Lee, J.-W. Activated carbon with hierarchical micro-mesoporous structure obtained from rice husk

https://doi.org/10.1021/acsaem.5c01629
ACS Appl. Energy Mater. 2025, 8, 12139−12156

and its application for lithium-sulfur batteries. *RSC Adv.* **2017**, *7* (7), 4144−4151.
(68) Schipper, F.; Vizintin, A.; Ren, J.; Dominko, R.; Fellinger, T. P. Biomass-derived heteroatom-doped carbon aerogels from a salt melt sol-gel synthesis and their performance in li-s batteries. *ChemSusChem* **2015**, *8* (18), 3077−3083.
(69) Wu, B.; Chen, F.; Mu, D.; Liao, W.; Wu, F. Cycleability of sulfurized polyacrylonitrile cathode in carbonate electrolyte containing lithium metasilicate. *J. Power Sources* **2015**, *278*, 27−31.
(70) Ren, J.; Zhou, Y.; Wu, H.; Xie, F.; Xu, C.; Lin, D. Sulfur-encapsulated in heteroatom-doped hierarchical porous carbon derived from goat hair for high performance lithium-sulfur batteries. *J. Energy Chem.* **2019**, *30*, 121−131.
(71) Li, X.; Banis, M.; Lushington, A.; Yang, X.; Sun, Q.; Zhao, Y.; Liu, C.; Li, Q.; Wang, B.; Xiao, W.; et al. A high-energy sulfur cathode in carbonate electrolyte by eliminating polysulfides via solid-phase lithium-sulfur transformation. *Nat. Commun.* **2018**, *9* (1), No. 4509.
(72) Li, G.; Jing, H.; Li, H.; Liu, L.; Wang, Y.; Yuan, C.; Jiang, H.; Chen, L. Sulfur/microporous carbon composites for Li-S battery. *Ionics* **2015**, *21*, 2161−2170.
(73) Zhang, J.; Dong, Z.; Wang, X.; Zhao, X.; Tu, J.; Su, Q.; Du, G. Sulfur nanocrystals anchored graphene composite with highly improved electrochemical performance for lithium-sulfur batteries. *J. Power Sources* **2014**, *270*, 1−8.
(74) Du, W. C.; Zhang, J.; Yin, Y. X.; Guo, Y. G.; Wan, L. J. Sulfur confined in sub-nanometer-sized 2D graphene interlayers and its electrochemical behavior In Lithium-Sulfur Batteries. *Chem. - Asian J.* **2016**, *11* (19), 2690−2694.
(75) Tougaard, S. Energy loss in XPS: Fundamental processes and applications for quantification, non-destructive depth profiling and 3D imaging. *J. Electron Spectrosc. Relat. Phenom.* **2010**, *178-179*, 128−153.
(76) Peled, E.; Menkin, S. Review—SEI: Past, Present and Future. *J. Electrochem. Soc.* **2017**, *164* (7), No. A1703.
(77) Yu, W.; Yu, Z.; Cui, Y.; Bao, Z. Degradation and speciation of Li salts during XPS analysis for battery research. *ACS Energy Lett.* **2022**, *7* (10), 3270−3275.
(78) Vizintin, A.; Lozinšek, M.; Chellappan, R. K.; Foix, D.; Krajnc, A.; Mali, G.; Drazic, G.; Genorio, B.; Dedryvère, R.; Dominko, R. Fluorinated reduced graphene oxide as an interlayer in Li-S batteries. *Chem. Mater.* **2015**, *27* (20), 7070−7081.
(79) García-Soriano, F. J.; Ceppi, S. A.; Cometto, F. P.; Primo, E. N.; Barraco, D. E.; Leiva, E. P. M.; Luque, G. L.; Stutz, G.; Lener, G.; Bracamonte, M. V. Sepiolite as a novel polysulfide trapper for energy applications: an electrochemical, X-ray spectroscopic and DFT study. *Phys. Chem. Chem. Phys.* **2023**, *25* (36), 24761−24769.
(80) Leckie, T. J.; Robertson, S. D.; Brightman, E. Recent advances in in situ/operando characterization of lithium sulfur batteries. *Energy Adv.* **2024**, *3* (10), 2479−2502.
(81) Baloch, M.; Shanmukaraj, D.; Bondarchuk, O.; Bekaert, E.; Rojo, T.; Armand, M. Variations on Li_3N protective coating using ex-situ and in-situ techniques for Li° in sulphur batteries. *Energy Storage Mater.* **2017**, *9*, 141−149.
(82) Mu, K.; Wang, D.; Dong, W.; Liu, Q.; Song, Z.; Xu, W.; Yao, P.; Chen, Ya.; Yang, B.; Li, C.; et al. Hybrid crosslinked solid polymer electrolyte via in-situ solidification enables high-performance solid-state lithium metal batteries. *Adv. Mater.* **2023**, *35* (47), No. 2304686.
(83) Gehrlein, L.; Njel, C.; Jeschull, F.; Maibach, J. From additive to cosolvent: how fluoroethylene carbonate concentrations influence solid-electrolyte interphase properties and electrochemical performance of Si/Gr anodes. *ACS Appl. Energy Mater.* **2022**, *5* (9), 10710−10720.
(84) Wang, Y.; Liu, Y.; Tu, Y.; Wang, Q. Reductive decomposition of solvents and additives toward solid-electrolyte interphase formation in lithium-ion battery. *J. Phys. Chem. C* **2020**, *124* (17), 9099−9108.
(85) Mokudai, H.; Takeuchi, T.; Sakaebe, H.; Kobayashi, H.; Matsubara, E. Degradation mechanisms of lithium sulfide (Li_2S) composite cathode in carbonate electrolyte and improvement by increasing electrolyte concentration. *Sustainable Energy Fuels* **2021**, *5* (6), 1714−1726.
(86) Liu, Q.; Sun, Y.; Wang, S.; An, Q.; Duan, L.; Zhao, G.; Wang, C.; Doyle-Davis, K.; Guo, H.; Sun, X. Highly adaptable SEI/CEI interfacial layers enabling remarkable performance of high-nickel solid-state batteries. *Mater. Today* **2023**, *64*, 21−30.
(87) Ni, X.; Qian, T.; Liu, X.; Xu, N.; Liu, J.; Yan, C. High lithium ion conductivity LiF/GO solid electrolyte interphase inhibiting the shuttle of lithium polysulfides in long-life Li-S Batteries. *Adv. Funct. Mater.* **2018**, *28* (13), No. 1706513.
(88) Tikekar, M. D.; Choudhury, S.; Tu, Z.; Archer, L. A. Design principles for electrolytes and interfaces for stable lithium-metal batteries. *Nat. Energy* **2016**, *1* (9), No. 16114.

https://doi.org/10.1021/acsaem.5c01629
ACS Appl. Energy Mater. 2025, 8, 12139−12156